

Properties and Expected Number Counts of Active Galactic Nuclei and their Hosts in the Far Infrared

A. R. Draper and D. R. Ballantyne

*Center for Relativistic Astrophysics, School of Physics, Georgia Institute of Technology,
Atlanta, GA 30332*

aden.draper@physics.gatech.edu

ABSTRACT

Telescopes like *Herschel* and the Atacama Large Millimeter/submillimeter Array (ALMA) are creating new opportunities to study sources in the far infrared (FIR), a wavelength region dominated by cold dust emission. Probing cold dust in active galaxies allows for study of the star formation history of active galactic nuclei (AGN) hosts. The FIR is also an important spectral region for observing AGN which are heavily enshrouded by dust, such as Compton thick AGN. By using information from deep X-ray surveys and cosmic X-ray background synthesis models, we compute Cloudy photoionization simulations which are used to predict the spectral energy distribution (SED) of AGN in the FIR. Expected differential number counts of AGN and their host galaxies are calculated in the *Herschel* bands. The expected contribution of AGN and their hosts to the cosmic infrared background (CIRB) and the infrared luminosity density are also computed. Multiple star formation scenarios are investigated using a modified blackbody star formation SED. It is found that FIR observations at $\sim 500 \mu\text{m}$ are an excellent tool in determining the star formation history of AGN hosts. Additionally, the AGN contribution to the CIRB can be used to determine whether star formation in AGN hosts evolves differently than in normal galaxies. The contribution of Compton thick AGN to the bright end differential number counts and to the bright source infrared luminosity density is a good test of AGN evolution models where quasars are triggered by major mergers.

Subject headings: galaxies: active — galaxies: evolution — galaxies: quasars: general — infrared: galaxies — X-rays: galaxies

1. Introduction

Thanks to the *Spitzer Space Telescope* and its imaging and spectroscopic instrument suite (Werner et al. 2004), it has recently been found that active galactic nuclei (AGN) can dominate the near and mid-infrared luminosity and make a significant contribution to the 8-1000 μm luminosity, L_{IR} , of AGN host galaxies (Houck et al. 2005; Yan et al. 2005; Weedman et al. 2006; Soifer et al. 2008, and references therein). Specifically, a large fraction of ultra-luminous infrared galaxies ($L_{\text{IR}} > 10^{12} L_{\odot}$; ULIRGs) and luminous infrared galaxies ($L_{\text{IR}} > 10^{11} L_{\odot}$; LIRGs) appear to host luminous AGN (e.g., Dey et al. 2008; Donley et al. 2008; Fiore et al. 2008, 2009; Yuan et al. 2010). In the far infrared (FIR) it is more difficult to determine the AGN contribution to the combined AGN and host observed flux as little is known about the AGN spectral energy distribution (SED) at these wavelengths. For the purposes of this study we define the FIR as 70-1000 μm .

The next several years will see a huge growth in high quality FIR and submillimeter spectral data due to telescopes like the *Herschel Space Observatory* and the Atacama Large Millimeter/submillimeter Array (ALMA). *Herschel*, launched in May 2009, offers unprecedented coverage of the FIR and submillimeter spectral regions (Pilbratt et al. 2010). *Herschel* carries two imaging photometers, the Photodetector Array Camera and Spectrometer (PACS) which has photometric bands at 70, 100, and 160 μm (Poglitsch et al. 2010) and the Spectral and Photometric Imaging Receiver (SPIRE) which has photometric bands at 250, 350, and 500 μm (Griffin et al. 2010). As one of the primary science goals of *Herschel* is to study the evolution of galaxies (Pilbratt et al. 2010), three wide-area surveys of various depths are being undertaken. The PACS evolutionary probe (PEP) will cover $\sim 3 \text{ deg}^2$ and will observe some fields, such as the GOODS fields, down to the depth of the 100 and 160 μm confusion limits of a few mJy (Berta et al. 2010). The *Herschel* Multi-tiered Extragalactic Survey (HerMES) will observe $\sim 70 \text{ deg}^2$ with SPIRE, reaching 5σ depths of a couple mJy at 250 μm in some fields (Oliver et al. 2010; Roseboom et al. 2010). Observing $\sim 510 \text{ deg}^2$ with both PACS and SPIRE, the *Herschel* Atlas (H-ATLAS) survey is the largest open time survey being undertaken by *Herschel* (Eales et al. 2010). H-ATLAS will reach 5σ depths of 67 mJy at 100 μm and 53 mJy at 500 μm (Eales et al. 2010; Ibar et al. 2010; Pascale et al. 2010). The ground-based instrument Submillimeter Common-User Bolometer Array 2 (SCUBA-2) will operate at 450 and 850 μm and will offer an intermediate sensitivity and mapping speed between those of *Herschel* and ALMA (Holland et al. 2006). Also ground-based, ALMA is an imaging and spectroscopic instrument operating in the millimeter and submillimeter regime. The ALMA primer¹ notes that at full science operations, starting

¹available at <http://www.almaobservatory.org/images/stories/publications>

in late 2012, ALMA will have a 450 μm band (Band 9) with a continuum sensitivity of 0.69 mJy and a 350 μm band (Band 10) with a sensitivity of 1.1 mJy, along with bands at longer wavelengths². The 450 μm band will be available for early science operations in mid 2011, albeit at reduced sensitivity. *Herschel*'s observing capabilities, and in particular the SPIRE deep and wide surveys at 250, 350 and 500 μm , will provide promising candidate targets for ALMA early science operations.

It is expected that AGN and their hosts will be readily detected in the FIR by *Herschel*. Hatziminaoglou et al. (2010) found that a third of their AGN sample had *Herschel* 5σ detections at 250 μm with $f_{250\mu\text{m}} > 12.8$ mJy, where $f_{250\mu\text{m}}$ is the 250 μm flux. The FIR flux from AGN and their hosts will be due to dust heated by a combination of AGN radiation and star formation. Observations suggest that only 3–9% of submillimeter galaxies are dominated by AGN emission in the submillimeter (Laird et al. 2010). However, a large portion of galaxies, nearly 50% of the galaxies in the infrared selected sample of Yuan et al. (2010), show strong infrared emission from both star formation and AGN activity. Consequently, the AGN contribution to the FIR emission of AGN hosts must be considered in order to not over-estimate star formation rates in AGN hosts.

As the FIR SED of AGN is expected to generally be dominated by star formation (e.g. Hatziminaoglou et al. 2010; Lutz et al. 2010), FIR observations will inform investigations of the star formation history of AGN hosts. By comparing the star formation history of AGN hosts and normal galaxies, the role of AGN in galaxy evolution will be constrained. Understanding AGN host star formation history is therefore an important tool in determining what processes trigger AGN. For example, Sanders et al. (1988) proposed that galaxy mergers trigger both intense starbursts and quasar activity. Recent observations and simulations support this model (Page et al. 2004; Hopkins et al. 2006; Rigopoulou et al. 2009; Draper & Ballantyne 2010; Kelly et al. 2010). Page et al. (2004) found that type 2 AGN tend to have higher SFRs than type 1 AGN. Draper & Ballantyne (2010) found that a significant fraction of Compton thick (CT) AGN, AGN with an X-ray obscuring column density $N_H > 10^{24} \text{ cm}^{-2}$, are quasars which are accreting very rapidly, as predicted by simulations by Hopkins et al. (2006) and others. However, it appears that this model may only be applicable for the most powerful AGN and that Seyfert strength AGN may evolve more secularly (Ballantyne et al. 2006a; Hasinger 2008; Lutz et al. 2010; Narayanan et al. 2010). In order to determine the applicability of the merger driven evolution and secular evolution models, the star formation history of AGN hosts must be accurately determined. This requires a robust method of identifying AGN hosts and the AGN contribution to the FIR emission.

²Sensitivities are for an integration time of 60 seconds and a spectral resolution of 1.0 km/s.

FIR emission from AGN comes from the "torus" of dusty gas, which, according to the unified scheme, surrounds the central engine of all AGN (e.g., Antonucci 1993). This dusty torus will absorb higher energy emission from the central engine of the AGN and re-radiate this energy in the infrared. The temperature of the dust, and therefore the peak wavelength of the infrared radiation, is dependent on the density of the obscuring gas and the distance of the obscuring gas from the central engine (e.g., Ballantyne et al. 2006b), among other parameters like the geometry of the obscuring torus (e.g., Hatziminaoglou et al. 2009). It appears that the infrared SED of most X-ray selected AGN peaks in the mid-infrared (e.g., Elvis et al. 1994; Netzer et al. 2007). However, due to the large amount of dust required to reach CT levels of obscuration, it is expected that the clouds of dusty gas in CT AGN will have a greater spatial extent than in less obscured AGN. Therefore, CT AGN will have a significant reservoir of dusty gas which is cooler than most AGN-related dust clouds. This cooler dust component will cause CT AGN to be brighter in the FIR than unobscured AGN.

Indeed, studies suggest that bright galaxies detected in the FIR host a large number of heavily obscured, $N_H > 10^{23} \text{ cm}^{-2}$, and possibly CT AGN (e.g., Alexander et al. 2005a,b; Bongiovanni et al. 2010; Wilman et al. 2010). Mullaney et al. (2010) found that 45–75% of the 1 Ms CDF-S X-ray sources will be detected by *Herschel* at $100 \mu\text{m}$ and that deep infrared observations with *Herschel* will allow for a significant fraction of the CT AGN population to be identified. Also, since X-ray selection misses nearly half of all infrared identified AGN (Fu et al. 2010) it is expected that FIR telescopes like *Herschel* and ALMA will detect highly obscured AGN that are missed by the deep X-ray surveys. However, there is an open debate as to how many of these infrared AGN reach CT levels of obscuration. Fiore et al. (2009) find that up to 90% of sources with $f_{24} > 550 \mu\text{Jy}$ and $f_{24}/f_R > 1000$ are CT AGN, where f_{24} is the $24 \mu\text{m}$ flux and f_R is the R-band flux. Conversely, Georgantopoulos et al. (2010) find a more moderate fraction of CT AGN for this population. When looking at similar infrared excess sources, Georgakakis et al. (2010) found no strong evidence suggesting that these sources host AGN with CT levels of obscuration. Therefore further study of the infrared properties of AGN are important in determining exactly how many CT AGN are hidden within dusty luminous infrared galaxies.

This work makes predictions for FIR AGN number counts, contribution to the CIRB, and luminosity density using a population synthesis model informed by constraints from the cosmic X-ray background (CXRB) and deep X-ray surveys, including the Eddington ratio dependent CT fraction, f_{CT} , of the composite model investigated by Draper & Ballantyne (2010). The effect of various AGN host star formation scenarios are also investigated. The calculation of the model SEDs is discussed in §2. Predictions for bare AGN are presented in §3 followed by predictions for various host star formation scenarios in §4. In §5 and §6 the results are discussed and summarized. A ΛCDM cosmology is assumed as necessary, with

$h_0 = 0.7$, $\Omega_m = 0.3$, and $\Omega_\Lambda = 0.7$ (Hinshaw et al. 2009).

2. Calculation of AGN SEDs

As the goal of this study is to make predictions of the average FIR properties of AGN, SEDs are used which are representative of an ensemble of AGNs at a given 2–10 keV luminosity, L_X , and z , instead of using a SED template based on observations of a statistically small set of AGNs. Since AGN IR emission is primarily due to the obscuring gas and dust re-radiating absorbed X-ray emission, photoionization simulations allow for the computation of the IR emission of an average AGN with a given L_X and N_H . Also, this SED computation method provides an opportunity to explore the parameter space of obscuring gas location, density distribution, and dust content, which, upon comparison with observations, may offer constraints for these physical parameters.

Similarly to Ballantyne et al. (2006b), the IR AGN SEDs are calculated using the photoionization code Cloudy version C08.00 (Ferland et al. 1998). Cloudy includes the complicated physics of radiative transfer through dusty gas and uses a physical dust model which takes into account silicate and graphite grains along with polycyclic hydrocarbons (PAHs). This technique does necessitate a simplification of the IR emitting region, which might actually be quite complex (e.g., Hatziminaoglou et al. 2009; Hönig et al. 2010). However, since our purpose is to describe average properties of AGN, and not to model individual objects, this technique is an appropriate method of SED calculation. This assumption will be tested by comparing the model SEDs against real data in §2.3.

2.1. Cloudy Model Setup

Each Cloudy model is setup such that a constant AGN spectrum, characterized by L_X , is incident upon a cloud with inner radius r from the continuum source. The inner radius r is set to 10 pc. Compton thin clouds are assigned a uniform hydrogen density $n_H = 10^4 \text{ cm}^{-3}$, as is typical of molecular clouds. In order to prevent the dust mass from becoming too large, the Compton thick clouds are assigned $n_H = 10^6 \text{ cm}^{-3}$. Molecular clouds of this density are not uncommon and have been observed in the Large Magellanic Cloud (Rubio et al. 2009) and in the Orion Nebula (Persson et al. 2007). Simulations were also run with $r = 1 \text{ pc}$ and $n_H = 10^4 \text{ cm}^{-3}$ for both Compton thin and CT clouds to test the sensitivity of the results to these assumptions, which is discussed later.

The Cloudy model input files are similar to those used by Ballantyne et al. (2006b), with

the following improvements. Instead of using a constant α_{OX} for all AGN, the Steffen et al. (2006) α_{OX} - L_{2keV} relation is used here to determine α_{OX} . The most significant improvement made includes dividing the AGN population into Eddington ratio bins, high ($L/L_{Edd} > 0.9$, where L is the bolometric luminosity found using the bolometric correction by Marconi et al. (2004) and L_{Edd} is the Eddington luminosity), moderate ($0.9 > L/L_{Edd} > 0.01$), and low ($0.01 > L/L_{Edd}$), as described by Draper & Ballantyne (2010). Both the composite and original models of Draper & Ballantyne (2010) are investigated. The f_{CT} of the composite model is Eddington ratio dependent and finds that $\sim 86\%$ of AGN accreting at greater than 90% of their Eddington rate and $\sim 60\%$ of AGN accreting at less than 1% of their Eddington rate are Compton thick. The original model assumes Compton thick AGN are a simple extension of the Compton thin type 2 population and that $\sim 44\%$ of type 2 AGN are Compton thick. Since the covering factor is set assuming the unified scheme holds, the covering factors are Eddington ratio dependent since f_{CT} is Eddington ratio dependent. For Compton thick objects the covering factor is set as the Compton thick fraction, f_{CT} . For objects with $22 \leq \log N_H < 24$ the covering factor is set as $(1.0 - f_{CT})f_2$ where f_2 is the type 2 fraction and is calculated as discussed in §2.2 of Draper & Ballantyne (2009). The covering factor for objects with $20 \leq \log N_H < 22$ is set to $(1.0 - f_{CT})(1.0 - f_2)$. As the covering factor is dependent on the Eddington ratio and varies from $z = 0$ to 1, Cloudy models had to be calculated as a function of z and L/L_{Edd} for each L_X and N_H .

There is evidence that different levels of obscuration in quasars might be related by an evolutionary scenario instead of by orientation effects (e.g., Sanders et al. 1988; Page et al. 2004; Draper & Ballantyne 2010; Donley et al. 2010), and thus the covering factor need not be related to f_{CT} or f_2 . Ballantyne et al. (2006b) found that the unified model assumption holds for lower luminosity quasars and Seyfert galaxies but does not seem to hold for high-luminosity quasars, possibly due to a different evolution for high luminosity, and therefore high Eddington ratio, quasars. Here this issue is addressed by using the Eddington ratio dependent f_{CT} of the composite model, which takes into account the different evolution of high Eddington ratio quasars from the moderate and low Eddington ratio AGN.

2.2. The Model Grids

As this investigation of the FIR properties of AGN is informed by the constraints offered by the CXRB and X-ray observations of AGN, SEDs are calculated as a function of $\log L_X$ and z . It is assumed that the redshift evolution of f_2 halts at $z = 1$, thus models are computed up to $z = 1$ and the $z = 1$ models are used at $z > 1$. Therefore, we compute Cloudy models for $z = 0$ to 1, in steps of 0.05, and $\log L_X = 41.5$ to 48, in steps of 0.25.

For each luminosity and redshift, Cloudy models are calculated for each $\log N_H = 20.0, 20.5, \dots, 24.5, 25.0 \text{ cm}^{-2}$. Since the covering factor is Eddington ratio dependent, Cloudy models had to be calculated for each luminosity, redshift, and column density for each of the three Eddington ratio bins. This resulted in 18711 individual Cloudy models for each r investigated and an additional 5103 Cloudy models to investigate the sensitivity of results to the hydrogen density, n_H , of the Compton thick clouds.

As we need to run 33 models for each (L_X, z) pair, it is computationally prohibitive to run models on a finer grid. Therefore, we have linearly interpolated between the SEDs to allow for a finer grid in the calculations. Thus eight SEDs are interpolated between consecutive $\log L_X$ model SEDs at a given z and two SEDs are interpolated between consecutive z model SEDs at a given L_X . A convergence test was conducted using twice as many steps in both L_X and z ; it was found that the step size used here is adequate for convergence.

To create final SEDs from the 18711 Cloudy models, we follow the method described by Ballantyne et al. (2006b). For each Eddington ratio bin, the weighted average of the reflection components of each N_H is added to the net transmitted continua of each N_H to create the "unified SEDs". The final SEDs are calculated in three categories: type 1, type 2 but Compton thin (which will be referred to as "type 2"), and Compton thick, for each Eddington ratio bin. The type 1 SED is an average of the $20 \leq \log N_H < 22$ unified SEDs, the type 2 SED is an average of the $22 \leq \log N_H < 24$ unified SEDs, and the CT SED is an average of the $24 \leq \log N_H$ unified SEDs. At this point, for each (L_X, z) pair there is a type 1, type 2, and Compton thick SED for each Eddington ratio bin. Figure 1 shows the rest frame $\log L_X = 43$ and $z = 0.45$ SEDs for the high Eddington ratio bin, which has $f_{CT} = 0.86$ and $f_2 = 0.78$.

2.3. Properties of AGN Model SEDs

The model SEDs were tested in the same manner as by Ballantyne et al. (2006b) to assure the assumptions used to compute the SEDs were appropriate and that the model SEDs are consistent with observed SED trends. As little is known about AGN FIR SEDs, these tests primarily investigate the mid-infrared properties of the model SEDs. The mid-infrared colors were examined and found to be consistent with the findings of Brand et al. (2006). The mid-infrared to X-ray flux ratio was considered as a function of N_H and no correlation was found, in agreement with observational data (Lutz et al. 2004; Rigby et al. 2004; Gandhi et al. 2009). Also, the fluxes were tested against and found to be consistent with expectations from local bright AGN, known as "Piccinotti AGNs" (see Alonso-Herrero et al. 2004). As our goal is to make predictions which characterize an ensemble of AGNs, like

number counts, the model SEDs are not compared against individual objects but against data which explores average properties of AGN SEDs. The model SEDs are found to be consistent with the observed AGN SED trends.

The model SEDs were also tested against the more recently discovered correlation between mid-infrared luminosity, $L_{12.3\mu m}$, and L_X for a sample of local Seyferts (Gandhi et al. 2009). Figure 2 compares the $z = 0.05$ model SEDs to the local best-fit correlation found by Gandhi et al. (2009). The model SEDs agree reasonably well with the correlation, especially the type 1 SEDs. At high luminosities the Compton thick SEDs appear to have a slight X-ray excess compared to the local Seyfert correlation. This is due to the Compton thick SEDs including more power radiated in the FIR, and consequently less power radiated in the mid-infrared, than the Compton thin SEDs. The $r = 1.0$ pc model SEDs do match the $L_{12.3\mu m} - L_X$ relation better than the $r = 10$ pc model SEDs; however, the $r = 10$ pc model SEDs best describe the general mid-infrared properties of an ensemble of AGN (see Ballantyne et al. 2006b). The fact that the $r = 1.0$ pc model SEDs fit this relation better than the $r = 10$ pc model SEDs shows that the distribution of gas and dust in the AGN dusty torus is an important effect in the mid-infrared. In order for the models used here to better approximate the Gandhi et al. (2009) relation, the geometry of the dusty torus should be carefully taken into account. The FIR SEDs are dominated by star formation, so the geometric details of the hot dust close to the central engine should not affect the results of this study. Also, as this study is focused on the integral properties of a large number of AGN, detailed modeling of the torus geometry is beyond the scope of this current study and we leave this for future work. Overall, the model SEDs are an appropriate representation of average AGN SEDs.

3. Predictions for Bare AGNs

In this section we present predictions for differential number counts, the AGN contribution to the cosmic infrared background (CIRB), and luminosity density, based on the model SEDs. The population synthesis model last described by Draper & Ballantyne (2010) is used to incorporate the information about and the constraints on the AGN population from deep hard X-ray surveys and the CXRB into infrared predictions.

3.1. Differential Number Counts

The number of sources per square degree with flux greater than S , $N(> S)$ is found by

$$N(> S) = \frac{K_{sr}^{deg} c}{H_0} \times \int_{z_{min}}^{z_{max}} \int_{\log L_X^{min}, \log L_X^S}^{\log L_X^{max}} \frac{d\Phi_\lambda(L_X, z)}{d \log L_X} \frac{d_l^2}{(1+z)^2 [\Omega_m(1+z)^3 + \Omega_\Lambda]^{1/2}} d \log L_X dz, \quad (1)$$

where the factor $K_{sr}^{deg} = 3.05 \times 10^{-4}$ converts from sr^{-1} to deg^{-2} , $d\Phi_\lambda(L_X, z)/d \log L_X$ is the evolving Eddington ratio space density computed by Draper & Ballantyne (2010), in Mpc^{-3} , d_l is the luminosity distance, and $\log L_X^S$ is the 2–10 keV rest-frame luminosity corresponding to the observed-frame infrared flux S at redshift z . The differential number counts are found by taking the derivative of $N(> S)$ with respect to S , $dN(> S)/dS$. The differential number counts were also calculated directly. However, due to the coarseness of the L_X and z grid used, the differential number counts contained numerical artifacts at brighter fluxes. The predictions from the two calculation methods are in agreement; however, computing the integral number counts on a very fine flux grid and then taking the derivative with respect to flux minimizes the numerical noise found in direct calculation of the differential number counts.

The Euclidean normalized differential number counts for 70, 100, 160, and 250 μm are shown in figure 3³. Plots are not shown for the 350 and 500 μm bands because, as evident in figure 1, the flux due to the AGN is very small at such long wavelengths; for example, at 10 mJy the 500 μm band $dN(> S)/dS \approx 0.4$ AGN hosts $\text{mJy}^{1.5} \text{deg}^{-2}$. The black lines show the predictions for the composite model and the cyan lines show the predictions for the original model. For ease in interpreting the figure, the low, moderate and high Eddington ratio bins have been combined and the total differential counts are shown (see §5.4 for a discussion about the contribution from the various Eddington ratio bins). As expected, the differential number counts for bare AGN are very small at long wavelengths because the AGNs tend to create hot dust. Therefore, long wavelengths can be used to investigate the star formation in AGN hosts. For both the original and composite models, CT AGN dominate the bright end of the differential counts, especially at wavelengths longer than 70 μm . In both models the type 2 AGN dominate at lower fluxes and the type 1 AGN contribute significantly less than their obscured counterparts at all wavelengths. The original model and composite model differential counts peak at about the same flux for each wavelength and have similar bright

³Fluxes are calculated at the filter nominal wavelengths. Using the full filter transmission function to calculate the dN/dS provides a result which is within a factor of 1.05 of that obtained when calculating the flux at the filter nominal wavelength. Thus the error due to calculating the fluxes at the filter nominal wavelength instead of using the full filter profile is negligible compared to the uncertainties in the model and the measurements.

end slopes. However, the original model peaks above the composite model and declines faster on the lower flux level end.

It is important to consider the dependence of these predictions on the parameters of the distance of the inner edge of the cloud from the ionizing source, r , and the n_H of the CT clouds, $n_{H,CT}$. As seen in figure 4, when $r = 1$ pc the differential counts are greatly reduced at all FIR wavelengths because the dust is hot and radiating more energy in the mid-infrared. Contrastingly, when $r > 10$ pc the differential counts are enhanced due to the dust being farther from the illuminating source and therefore cooler. Similarly, when $n_{H,CT} = 10^4 \text{ cm}^{-3}$ the differential counts are slightly enhanced in the FIR due to the greater spatial extent of the cloud. However, since the combined AGN and host SED will be dominated by star formation at longer wavelengths, and there is likely to be variation among individual objects, the exact values for r and $n_{H,CT}$ used will have little effect on the final predictions.

3.2. CIRB

The AGN contribution to the CIRB is calculated similarly to population synthesis models looking at the CXRB, but exchanging the X-ray spectrum with the infrared spectrum. Thus we have

$$I_\nu(\nu) = \frac{c}{H_0} \int_{z_{min}}^{z_{max}} \int_{\log L_X^{min}}^{\log L_X^{max}} \frac{d\Phi_\lambda(L_X, z)}{d \log L_X} \times \frac{S_\nu(L_X, z) d_l^2}{(1+z)^2 [\Omega_m(1+z)^3 + \Omega_\Lambda]^{1/2}} d \log L_X dz, \quad (2)$$

where $S_\nu(L_X, z)$ is the observed-frame AGN model SED, in Jy sr⁻¹, computed with L_X at redshift z . As there is little knowledge about the SEDs of AGN in the FIR, there are very few constraints on the AGN contribution to the CIRB. Jauzac et al. (2010) claim that AGN contribute $\lesssim 10\%$ of the CIRB at $z < 1.5$, based on *Spitzer* observations in the GOODS and COSMOS fields. By extrapolating from CXRB models to the CIRB using rough AGN SED templates, Silva et al. (2004) predict that bare AGN contribute $\sim 0.3\%$ of the CIRB at $160 \mu\text{m}^4$. Using a method similar to the one described here, Ballantyne & Papovich (2007) predict that bare AGN contribute $\sim 0.9\%$ of the CIRB at $160 \mu\text{m}$. Here it is found that both the composite and original models predict that bare AGN contribute $\sim 0.9\%$ of the CIRB at $160 \mu\text{m}$. As seen in figure 5, type 2 AGN dominate the CIRB at lower wavelengths and at higher wavelengths CT AGN dominate the AGN contribution to the CIRB. At wavelengths greater than $\sim 100 \mu\text{m}$ the original model and the composite model predict very similar contributions of AGN to the CIRB. Below $\sim 100 \mu\text{m}$ the composite model predicts a higher contribution to the CIRB by AGNs than the original model.

⁴Here we assume the intensity of the CIRB at $160 \mu\text{m}$ is $12.84 \text{ nW m}^{-2} \text{ sr}^{-1}$ (Altieri et al. 2010).

3.3. Luminosity Density

The cosmic infrared luminosity density and its evolution are good indicators of the star formation rate density and the evolution of star formation in the universe. However, infrared luminosity density is significantly contaminated by AGN, thus making it important to understand the contribution of AGN to the infrared luminosity density and how the AGN contribution to the infrared luminosity density evolves. The 8–1000 μm AGN luminosity density, ρ_{IR} , is calculated as

$$\rho_{IR}(z) = \int_{L_{IR,min}}^{L_{IR,max}} L_{IR} \frac{d\Phi_{\lambda}(L_{IR}, z)}{d \log L_{IR}} d \log L_{IR}, \quad (3)$$

where $d\Phi_{\lambda}/d \log L_{IR}$ is the evolving Eddington ratio space density calculated in Draper & Ballantyne (2010) in terms of the total infrared luminosity, i.e. a total infrared luminosity function for a population of AGN with a specific Eddington ratio, which is found using the relation

$$\frac{d\Phi_{\lambda}(L_{IR}, z)}{d(\log L_{IR})} = \frac{d\Phi_{\lambda}(L_X, z)}{d(\log L_X)} \frac{d(\log L_X)}{d(\log L_{IR})}. \quad (4)$$

As seen in figure 6, both the composite and original models are in agreement with observations by Goto et al. (2010a) at $z \approx 0.2$ – 0.8 . For $z \gtrsim 1$ both models do not evolve fast enough to agree with the ρ_{IR} and ULIRG AGN infrared luminosity density, ρ_{IR}^{ULIRG} . However, both models are in fairly good agreement with the high redshift LIRG AGN luminosity density, ρ_{IR}^{LIRG} . Locally both the original and composite model under-predict the ρ_{IR} and over-predict the ρ_{IR}^{ULIRG} , but are in agreement with the ρ_{IR}^{LIRG} , as measured by Goto et al. (2010b). Due to the method used to separate the AGN and star forming galaxies in the samples of Goto et al. (2010a,b), there is an uncertainty of up to 50% due to the complication of galaxies whose infrared SED is not clearly dominated by AGN activity nor by star formation (Goto et al. 2010b). Also, by applying the same method of separating the contribution of AGN and star forming galaxies to the infrared luminosity density measured by Le Floc’h et al. (2005) using *Spitzer* 24 μm sources in the CDF-S, the local ρ_{IR}^{ULIRG} is ~ 0.4 dex higher and in good agreement with local ρ_{IR}^{ULIRG} predicted here.

4. Accounting for Star Formation

The infrared SEDs of most AGN are dominated by star formation (e.g., Franceschini et al. 2010). Unless the AGN host galaxy can be spatially resolved, it is very difficult to separate the AGN emission from the star formation emission. Therefore it is important to consider how various AGN star formation scenarios will affect the predictions discussed above. In particular, a constant star formation rate is considered, keeping with the unified scheme. A star

formation scenario consistent with the AGN evolution scenario discussed by Sanders et al. (1988) is also analyzed. Finally, star formation scenarios which include evolution of the SFR with redshift and AGN L_X are considered.

To calculate the star formation SED for a given SFR, a modified black body spectrum characterized by the dust emissivity, β , and the dust temperature, T_d , is used. The Kennicutt (1998) relation,

$$SFR = 4.5 \times 10^{-44} L_{IR}, \quad (5)$$

is used to determine L_{IR} , in erg s^{-1} , for a given SFR, in $\text{M}_\odot \text{ yr}^{-1}$, and the L_{IR} - T_d relation from Amblard et al. (2010),

$$T_d = T_0 + \alpha \log(L_{IR}/L_\odot), \quad (6)$$

is used to determine T_d . Using *Herschel* observations, Amblard et al. (2010) find $T_0 = 20.5 \text{ K}$ and $\alpha = 4.4$, using $\beta = 1.5$. Amblard et al. (2010) define L_{IR} as the 8–1100 μm luminosity, instead of the 8–1000 μm luminosity as done here; however, for our purposes, the difference is negligible. The resulting star formation SEDs are in good agreement with the star formation templates presented by Rieke et al. (2009) at rest frame wavelengths greater than 50 μm . The star formation SEDs are then added to the model SEDs discussed above to create the AGN+SF SED. The calculations discussed in section §3 are repeated using the AGN+SF SEDs in place of the AGN model SEDs. Here, the predictions for the composite model are presented. A comparison of the predictions of the original and composite models is discussed in §5.2.

4.1. Constant Star Formation

The simplest star formation scenario is where AGN hosts have a constant SFR. Ballantyne & Papovich (2007) found that an average AGN $SFR = 1.0 \text{ M}_\odot \text{ yr}^{-1}$ reproduces the AGN contribution to the mid-infrared portion of the CIRB as measured by *Spitzer*; thus for the constant star formation model we set $SFR = 1.0 \text{ M}_\odot \text{ yr}^{-1}$. In keeping with the unified scheme, all AGN have the same SFR regardless of spectroscopic type. The Euclidean normalized differential number counts for the constant star formation model are shown as the black lines in figures 7, 8, 9, 10, 11, and 12. At wavelengths shorter than 350 μm , the number counts increase steeply from 0.01 mJy to $\sim 1 \text{ mJy}$ and then remain approximately flat through $\sim 25 \text{ mJy}$. At wavelengths longer than 350 μm , the number counts turn over around 1 mJy and continue to decrease toward brighter flux levels. At all wavelengths the CT AGN dominate the bright end counts above $\sim 1 \text{ mJy}$, with type 2 AGN dominating at lower flux levels.

The black lines in figure 13 show the AGN contribution to the CIRB for the constant

star formation model. In this star formation scenario, AGN contribute $\sim 4\%$ of the CIRB at $160\ \mu\text{m}$. The AGN contribution to the CIRB is dominated by CT AGN above $100\ \mu\text{m}$ and type 2 AGN also contribute significantly. The AGN contribution to the CIRB peaks at approximately the same wavelength as the CIRB itself peaks, $\sim 160\ \mu\text{m}$.

The ρ_{IR} is shown in figure 14, with the constant star formation model shown as the black lines. The ρ_{IR}^{ULIRG} is not increased over the bare AGN scenario, however, the total and LIRG AGN infrared luminosity densities are increased slightly. Thus the constant star formation model does not allow for rapid enough evolution with redshift to match the observed high redshift ρ_{IR} .

4.2. AGN Evolution Scenario

It has been suggested that, at least in the quasar regime, the level of obscuration observed in an AGN is connected to the evolutionary stage of the quasar (e.g., Sanders et al. 1988; Page et al. 2004; Ballantyne 2008; Draper & Ballantyne 2010). Galaxy merger simulations support the evolutionary scenario showing that gas rich mergers lead to a burst of star formation and intense, highly obscured black hole growth (e.g., Hopkins et al. 2006). In the AGN evolution scenario, high Eddington ratio CT AGN would be expected to have SFRs reaching into the ULIRG regime and type 2 AGN hosts would be expected to have more star formation than type 1 AGN hosts (e.g., Page et al. 2004). Following this prescription we set the high Eddington ratio $\text{SFR} = 175\ \text{M}_{\odot}\ \text{yr}^{-1}$, the type 2 $\text{SFR} = 2.0\ \text{M}_{\odot}\ \text{yr}^{-1}$, and type 1 $\text{SFR} = 0.5\ \text{M}_{\odot}\ \text{yr}^{-1}$. The low Eddington ratio CT AGN are also given $\text{SFR} = 0.5\ \text{M}_{\odot}\ \text{yr}^{-1}$ as these are weak AGN most likely obscured by molecular clouds in the host bulge or by dust lanes in the host galaxy (Martínez-Sansigre 2009), and not by intense nuclear starbursts. This star formation scenario gives predictions which are only negligibly different from the scenario where all AGN have $\text{SFR} = 1.0\ \text{M}_{\odot}\ \text{yr}^{-1}$ except for the high Eddington ratio CT AGN which have $\text{SFR} = 175\ \text{M}_{\odot}\ \text{yr}^{-1}$.

The Euclidean normalized differential counts for the AGN evolution scenario are shown as the green lines in figures 7, 8, 9, 10, 11, and 12. At all wavelengths the number counts rise as the flux level increases, leveling off around 1 mJy, and then continue to rise at least until the flux level of 10 mJy. CT AGN dominate at flux levels greater than ~ 6 mJy and type 2 AGN dominate at lower flux levels for all wavelengths.

In figure 13, the AGN contribution to the CIRB for the AGN evolution scenario is shown in green. At $160\ \mu\text{m}$, AGN contribute $\sim 6\%$ of the CIRB. CT AGN dominate the AGN contribution to the CIRB at wavelengths greater than $\sim 200\ \mu\text{m}$ and type 2 AGN

dominate below $200\ \mu\text{m}$. The peak of the AGN contribution to the CIRB is roughly at the same wavelength as the peak of the CIRB.

The green lines in figure 14 show the ρ_{IR} for the AGN evolution scenario. The total ρ_{IR} is in decent agreement with observations except at the highest redshift bin, which this model under-predicts. The local ρ_{IR}^{LIRG} and ρ_{IR}^{ULIRG} are over-predicted by this model but are in good agreement with observations at higher redshifts. However, the ρ_{IR}^{ULIRG} observations show a stronger redshift evolution than predicted by this model.

4.3. Evolution with Redshift

Also considered was the star formation redshift evolution found by Serjeant et al. (2010), where $\text{SFR} \propto (1.0+z)^{2.3}$. Serjeant et al. (2010) did find that the highest luminosity quasars had a much stronger redshift evolution, perhaps as strong as $\text{SFR} \propto (1.0+z)^{10}$. For simplicity the total volume-averaged star formation rate redshift evolution is used here, independent of the object luminosity. The local star formation rate is set such that $\text{SFR}(z=0.0) = 0.5\ \text{M}_{\odot}\ \text{yr}^{-1}$, in keeping with the average type 1 SFR found in a sample of local SDSS quasars by Kim et al. (2006). Following the unified scheme, the SFR is not dependent on spectroscopic type.

As shown by the red lines in figures 7, 8, 9, 10, 11, and 12, the Euclidean normalized differential number counts increase with increasing flux level until peaking at $\sim 1\ \text{mJy}$. The number counts decrease at flux levels above $\sim 1\ \text{mJy}$, and, for wavelengths greater than $160\ \mu\text{m}$, the number counts decrease more steeply as the wavelength increases. CT AGN dominate the counts on the brighter side of the peak and type 2 AGN dominate the lower flux level side of the peak.

The star formation redshift evolution model contribution to the CIRB is shown in red in figure 13. The AGN contribution to the CIRB at $160\ \mu\text{m}$ is $\sim 5\%$. CT AGN dominate the AGN contribution to the CIRB at wavelengths greater than $\sim 100\ \mu\text{m}$, with type 2 AGN dominating at lower wavelengths. The AGN contribution to the CIRB for this model peaks at $\sim 320\ \mu\text{m}$, a significantly longer wavelength than the peak of the CIRB as a whole.

The ρ_{IR}^{LIRG} and ρ_{IR}^{ULIRG} for the star formation redshift evolution model are very similar to those for the constant star formation scenario, as shown by the red lines in figure 14. The total ρ_{IR} of the star formation redshift evolution model under-predicts the observed local ρ_{IR} but evolves more strongly with redshift than the constant star formation scenario.

4.4. Evolution with Redshift and AGN L_X

The final star formation scenario investigated here is the redshift and AGN L_X dependent star formation scenario used by Wilman et al. (2010), where

$$SFR \propto \sqrt{L_X/10^{43}}(1.0 + z)^{1.6}. \quad (7)$$

Type 1 AGN are given the normalization constant $0.63 \text{ M}_\odot \text{ yr}^{-1}$ and for type 2 AGN the normalization prefactor is increased to $2.0 \text{ M}_\odot \text{ yr}^{-1}$ (Wilman et al. 2010). High Eddington ratio CT AGN are given the type 2 SFR and low Eddington ratio CT AGN are given the type 1 SFR, for the reasons discussed in §4.2.

The Euclidean normalized differential number counts for the redshift and AGN L_X dependent SFR model are shown as blue lines in figures 7, 8, 9, 10, 11, and 12 and are in decent agreement with the predictions made by Wilman et al. (2010) based on a simulation of the extragalactic radio sky. The differential number counts increase with increasing flux level until peaking at 1–3 mJy, depending on wavelength. The peak of the number counts appears to increase with wavelength, with the peak at ~ 1 mJy at $100 \mu\text{m}$ and ~ 3 mJy at $350 \mu\text{m}$. The number counts decrease from the peak to the brighter flux levels. At 100, 350, and $500 \mu\text{m}$ CT AGN dominate the number counts on the brighter side of the peak, but at 70, 160, and $250 \mu\text{m}$ type 2 AGN dominate except for at the brightest flux levels, $\gtrsim 10$ mJy.

The blue lines in figure 13 show the AGN contribution to the CIRB for the redshift and AGN L_X dependent SFR model. This model predicts $\sim 5\%$ of the CIRB at $160 \mu\text{m}$ is due to AGN. Type 2 AGN dominate the AGN contribution to the CIRB at all wavelengths and CT AGN make a significant contribution. For this model the AGN contribution to the CIRB peaks at $\sim 300 \mu\text{m}$, which is significantly different from the peak of the total CIRB around $160 \mu\text{m}$.

In figure 14 the ρ_{IR} for the redshift and L_X dependent SFR model is shown in blue. This model is in decent agreement with the ρ_{IR}^{LIRG} at all redshifts but over-predicts the local ρ_{IR}^{ULIRG} and under-predicts the local total ρ_{IR} . Both the total ρ_{IR} and ρ_{IR}^{ULIRG} predictions are in agreement with observations at moderate redshifts, but do not evolve strongly enough with redshift to be in agreement with observations at the highest redshift.

5. Discussion

We have presented predictions for observations of AGN and AGN hosts in the FIR *Herschel* bands based on the composite model by Draper & Ballantyne (2010)⁵. These findings demonstrate that while AGN may not contribute a large fraction of the CIRB, AGN will be significant FIR sources and care must be taken in FIR surveys to identify AGNs as such. Here we discuss the implications of these results in terms of AGN and AGN host demographics.

5.1. CT AGN

A substantial population of CT AGN are necessary for AGN population synthesis models to match the peak of the CXRB at ~ 30 keV (e.g., Ballantyne et al. 2006a; Treister et al. 2009a; Draper & Ballantyne 2010). Due to the extreme levels of obscuration in CT AGN, these elusive sources are generally only observed in the very hard X-ray, > 10 keV, or the infrared, especially the FIR. Using X-ray stacking methods, it has been shown that a large fraction of bright infrared excess sources ($f_{24}/f_R > 1000$) host heavily obscured AGN (e.g., Daddi et al. 2007; Fiore et al. 2009; Treister et al. 2009b). However, it is uncertain how many of these highly obscured AGN are actually CT (see Georgakakis et al. 2010; Georgantopoulos et al. 2010). Also, there is much debate over the prevalence of AGN in sources with more moderate infrared luminosities (e.g., Dey et al. 2008; Donley et al. 2008; Fiore et al. 2009; Treister et al. 2009b, 2010). Because CT AGN are generally not observable in the 2–10 keV band, AGN hard X-ray luminosity functions do not include CT AGN and therefore they must be added in by hand to population synthesis models. In the population synthesis model used in this study, CT AGN are assumed to be accreting at either at $L/L_{Edd} > 0.9$ or $L/L_{Edd} < 0.01$, with f_{CT} independent of f_2 , as found by Draper & Ballantyne (2010). Here we discuss predictions specifically for CT AGN in the FIR.

At all wavelengths and for all star formation scenarios, the differential number counts are dominated by CT AGN for fluxes $\gtrsim 1$ –10 mJy. Type 2 AGN dominate at lower fluxes. Moreover, CT AGN, should constitute a non-trivial fraction of *Herschel* sources. Depending on the star formation scenario considered, CT AGN could make up $\sim 10\%$ of *Herschel* sources, even at $500 \mu\text{m}$.

Depending on the star formation scenario, CT AGN are found to contribute $< 5\%$ of the CIRB at $160 \mu\text{m}$. For bare AGN, CT AGN dominate the AGN contribution to the CIRB

⁵Models are available in table form by contacting the authors.

at wavelengths $\gtrsim 200 \mu\text{m}$. When star formation is included, CT AGN dominate the AGN contribution to the CIRB at wavelengths $\gtrsim 100 \mu\text{m}$ for all star formation scenarios, except the Wilman et al. (2010) model.

Comparing the predictions made here against the infrared luminosity density found by Le Floc’h et al. (2005), we find that CT AGN and their hosts contribute $\sim 3\%$ of the local infrared luminosity density from sources with $L_{IR} > 10^{10} L_{\odot}$ and nearly one-fourth of the infrared luminosity density from sources in the ULIRG range. In the AGN evolution star formation scenario, CT AGN can account for all of the local ULIRG range luminosity density. At $z \sim 1$ the relative CT AGN contribution decreases significantly in all luminosity ranges. However, when taking into account the stronger evolution of the SFR in high luminosity sources found by Serjeant et al. (2010), CT AGN and their hosts can still contribute nearly a quarter of the infrared luminosity density in the ULIRG range at $z \sim 1$. Showing that at higher redshifts CT AGN contribute less to the total infrared luminosity density, but may still contribute quite significantly to the brightest sources.

The FIR is an important wavelength range for observing CT AGN due to the large amount of cold dust which obscures CT AGN. The majority of AGN observed by *Herschel* will be CT. Depending on the star formation trends in CT AGN hosts, CT AGN and their hosts may constitute nearly $\sim 10\%$ of *Herschel* sources at $500 \mu\text{m}$. The relative contribution of CT AGN and their hosts to the ULIRG range infrared luminosity density is $\lesssim 25\%$ and appears to be approximately constant over the redshift range $z = 0-1$. However, Hatziminaoglou et al. (2010) showed that AGN cannot be identified by their *Herschel*-SPIRE colors alone. Therefore finding CT AGN in the FIR will require either *Spitzer*-MIPS coverage of bright SPIRE sources (Hatziminaoglou et al. 2010) or X-ray stacking. Since the AGN and host differential number counts for both the composite and original models are dominated by CT AGN in the SPIRE bands, X-ray stacking of bright SPIRE sources is likely to disclose a large fraction of the CT AGN population.

5.2. Differences Between Original and Composite Model

The difference between the original model and the composite model is that in the composite model the CT AGN are put in specific, physically motivated Eddington ratio bins. Also, in the original model $f_{CT} \propto f_2$, but in the composite model f_{CT} is independent of f_2 . In order to understand the effects of the differences between the two models, we compare the predictions of the original and composite model for the constant star formation scenario.

In the differential number counts, the differences between the composite and original

models are small but not insignificant. At all wavelengths the original model has a steeper decline in the bright end counts than the composite model. The original model predicts that the number counts will be dominated by type 2 AGN except for at the brightest fluxes. Conversely, in the composite model the differential counts are dominated by CT AGN at every wavelength for fluxes $\gtrsim 1$ mJy.

The original model predicts a smaller overall AGN contribution to the CIRB than the composite model. In the composite model, CT AGN dominate the AGN contribution to the CIRB at wavelengths greater than $100 \mu\text{m}$, but in the original model the type 2 AGN dominate the AGN contribution to the CIRB at all wavelengths.

The original and composite models make similar predictions as to the AGN contribution to the infrared luminosity density in all luminosity ranges. The difference between these two models is most noticeable in the contribution of CT AGN to the local ULIRG range luminosity density. The original model predicts that CT AGN contribute 4% of the local ULIRG infrared luminosity density. The composite model predicts that nearly one-fourth of the local ULIRG infrared luminosity density is due to CT AGN.

The overall predictions of the original and composite models are in agreement. To observationally determine which model best describes the CT AGN population, rigorous measurements of the CT AGN contribution to the local infrared luminosity density and/or accurate accounting of *Herschel* number counts to see whether CT AGN or type 2 AGN dominate the number counts will be needed.

5.3. Star Formation in AGN hosts

As seen in figures 7, 8, 9, 10, 11, and 12, the star formation scenario used greatly affects the predicted differential number counts. At wavelengths $\lesssim 250 \mu\text{m}$, the faint end slope is similar for all the star formation models investigated here, but the bright end slope is highly dependent on the host star formation at all wavelengths. The differences between the various star formation scenarios becomes more prominent when observing at longer wavelengths. The constant star formation model peaks at ~ 1 mJy and has a relatively flat bright end slope. The AGN evolution star formation model peaks at $\gtrsim 10$ mJy with a knee at ~ 1 mJy. The redshift only evolution model peaks around, or just short of 1 mJy. This model also has the steepest faint and bright end slopes of the star formation scenarios considered here. The Wilman et al. (2010) star formation model peaks between 1 and 10 mJy for wavelengths $\gtrsim 100 \mu\text{m}$. The flux level of the peak in the differential counts may be an important tool in understanding the evolution of SFR in AGN hosts. This tool will be most effective when

observing at longer wavelengths.

Dust obscured star formation is believed to be the primary progenitor of the CIRB with much debate as to the contribution from AGN. Ballantyne & Papovich (2007) found that AGN and star formation in AGN hosts can account for $\sim 30\%$ of the CIRB at $70\ \mu\text{m}$. Similarly, Mullaney et al. (2010) find that AGN contribute 5–25% of the CIRB at $70\ \mu\text{m}$. However, at longer wavelengths it appears the AGN contribution reduces to $\lesssim 10\%$ (Jauzac et al. 2010; Lacey et al. 2010). In this work it was found that AGN and host star formation contribute $\sim 5\%$ of the CIRB at $160\ \mu\text{m}$. However, when investigating the submillimeter properties of X-ray-selected AGN, Lutz et al. (2010) found the average AGN SFR to be $\sim 30\ \text{M}_\odot\ \text{yr}^{-1}$, in which case AGN and their hosts would contribute $\sim 88\%$ of the CIRB at $160\ \mu\text{m}$. Therefore, understanding the star formation trends in AGN hosts is necessary for understanding how significant the contribution of AGN and their hosts is.

The peak intensity of the CIRB occurs at $\sim 160\ \mu\text{m}$. The star formation scenarios investigated here which take into account the evolution of the SFR with redshift predict the peak of the AGN contribution to the CIRB occurs at $\sim 300\ \mu\text{m}$. This suggests that the SFR of AGN hosts evolves differently with redshift than the SFR of normal galaxies. This effect could also be explained if the star formation SEDs used here are on average too cold, which is unlikely. If it is true that the SFR of AGN hosts evolves differently than the SFR of normal galaxies, this could offer important insights into the role of the AGN in the host galaxy evolution. At wavelengths shorter than the peak of the CIRB, the dominate contribution is from sources $z < 1$. Sources at $z > 2$ tend to dominate at wavelengths longer than $500\ \mu\text{m}$.

Another tool used to study different AGN host star formation scenarios is the infrared luminosity density. Using simulations, Hopkins et al. (2010) find that AGN contribute 1-5% of the total infrared luminosity density at all redshifts. Applying the classification scheme of Yuan et al. (2010) to AKARI sources, Goto et al. (2010b) find that AGN contribute $\sim 20\%$ of the total infrared luminosity density, $\sim 40\%$ of the luminosity density from sources in the LIRG range, and $\gtrsim 90\%$ of the luminosity density of sources in the ULIRG range, regardless of redshift. When considering the infrared luminosity density as measured by Le Floc’h et al. (2005), we find that the AGN and host galaxy contribution to the local infrared luminosity density is approximately a factor of 2 smaller than that found by Goto et al. (2010b). At $z \sim 1$ the relative AGN contribution decreases to $\lesssim 5\%$ for all luminosity ranges. Even when taking into account the stronger evolution of the SFR in high luminosity sources found by Serjeant et al. (2010), it appears that AGN and their hosts only contribute $\sim 25\%$ of the infrared luminosity density in the ULIRG luminosity range at $z \sim 1$. The reduction in the AGN contribution to the ULIRG range infrared luminosity density by a factor of 2 between $z \sim 0$ and $z \sim 1$, is consistent with the findings of Sturm et al. (2010) that ULIRG level

luminosities can be achieved without major mergers at higher redshifts, suggesting that the AGN fraction in the high redshift ULIRG population will be smaller than that found locally.

Determining the star formation history of AGN hosts is important in understanding why some galaxies host active supermassive black holes (SMBHs) and other galaxies host inactive SMBHs. The predictions presented here show that the flux level of the differential number counts peak in longer wavelength bands will be a helpful tool in determining the star formation history of AGN hosts. By comparing the peak wavelength of the AGN contribution to the CIRB to the peak wavelength of the CIRB, it is possible to determine if the star formation evolution of AGN hosts is different from that of normal galaxies. Also, at higher redshift AGN will have a smaller contribution to the ULIRG population, and that contribution will be dominated by CT AGN.

5.4. Eddington Ratio Breakdown

By using $d\Phi_\lambda(L_X, z)/d\log L_X$, the evolving Eddington ratio space density computed by Draper & Ballantyne (2010), instead of a traditional luminosity function, it is possible to make predictions for the contribution of AGN with different Eddington ratios. In figures 15 and 16 the composite model Euclidean normalized differential counts are shown for the AGN evolution star formation model at 160 and 500 μm with the relative contributions from the different Eddington ratio bins shown. The blue lines show the contribution from AGN with $L/L_{Edd} < 0.01$. The green lines show the contribution from AGN with $0.01 < L/L_{Edd} < 0.9$. The contribution from high Eddington ratio sources is shown in red. For all but the AGN evolution scenario, the number counts are dominated by low Eddington ratio AGN at all flux levels, due to the high space density of low accretion rate AGN at all redshifts. As shown in figures 15 and 16, the AGN evolutionary scenario bright end counts are dominated by high Eddington ratio CT AGN because of the high star formation rate in these objects.

For all star formation scenarios the low Eddington ratio sources dominate the AGN contribution to the CIRB at wavelengths $\gtrsim 100 \mu\text{m}$. The AGN contribution to the infrared luminosity density is dominated by moderate Eddington ratio AGN at all luminosity levels for all star formation scenarios except the AGN evolution star formation model, where the high Eddington ratio sources dominate the ULIRG range. The star formation scenarios that do not include redshift evolution find that low Eddington ratio sources dominate the AGN contribution to the local infrared luminosity density.

5.5. Implications for *Herschel* and ALMA

The three wide area surveys conducted by *Herschel* will yield a large catalog of AGN host galaxies. Using the planned survey depths and areas as described in Section 1, the models discussed here predict the following numbers of AGN hosts to be observed by the *Herschel* wide field surveys. Not including the planned lensing cluster observations, PEP should observe 100-500 AGN hosts, depending on the star formation scenario, at 160 μm with 5σ significance. The portion of HerMES conducted during the *Herschel* science demonstration phase should provide 140-2100 AGN hosts, depending on the star formation scenario, with 5σ significance at 250 μm . The H-ATLAS survey will yield 250-4000 AGN hosts at 160 μm and 90-1200 AGN hosts at 350 μm with 5σ significance. The H-ATLAS observed AGN host counts drop to 30-230 in the 500 μm band. This catalog of sources will provide a robust sample to better constrain the star formation properties of AGN hosts.

Hatziminaoglou et al. (2010) showed that AGN cannot be differentiated from normal galaxies based only on their FIR colors; therefore, ALMA will only be able to offer supplementary data on AGN which are identified in other wavelength bands. The wide area surveys conducted by *Herschel* will provide many promising candidate targets for ALMA. The dotted grey lines in figures 11 and 12 show the sensitivity limit of the 350 and 450 μm ALMA bands, respectively, as quoted in section 1. Based on this projected sensitivity and the models presented here, the areal density of AGN hosts available to ALMA at 450 μm will be 300-1500 deg^{-2} , depending on the star formation scenario, for an integration time of only 60 seconds. Therefore, using ALMA to conduct follow up observations on X-ray selected AGN should be an efficient way to study star formation in AGN host galaxies. As discussed in section 5.3, the differential number counts for different star formation scenarios seem to peak at different flux levels. These peak fluxes become more differentiated at higher wavelengths. By providing deeper submillimeter observations of *Herschel* sources and X-ray selected AGN, ALMA should be able to determine the evolution of star formation in AGN hosts. This will allow the determination of the wavelength where the AGN contribution to the CIRB peaks, and therefore whether the star formation in AGN hosts evolves differently than in normal galaxies. Furthermore, since ALMA will be taking spectra, measurements such as gas velocity, abundances, and temperature can be made. This will allow ALMA to not only determine the evolution of star formation in AGN hosts, but also to probe the physical structure of AGN host galaxy star formation.

5.6. Evolution of AGN

From deep X-ray surveys it is known that high luminosity quasars and moderate luminosity AGN evolve differently with respect to redshift (e.g., Ueda et al. 2003). This would suggest that quasars and Seyferts are caused by processes with different time scales. Also, it appears that the Seyfert population is well described by the unified scheme, but the high luminosity AGN population may not follow the unified model (e.g., Ballantyne et al. 2006b; Lutz et al. 2010). A picture is starting to surface where the most powerful AGN are triggered by major mergers as explored in the simulations by Hopkins et al. (2006) and others, but most AGN are triggered by less violent processes (Ballantyne et al. 2006a). This picture is taken into account here by using the composite model of Draper & Ballantyne (2010) to describe the CT AGN fraction as Eddington ratio dependent. The difference in triggering process will also affect the star formation within the host galaxy. Mergers will engender not only AGN activity but also bursts of star formation. Where as the more secular evolution experienced by moderate power AGN will induce moderate, constant star formation.

This AGN evolution scenario was further explored here with the AGN evolution star formation scenario. In this scenario, high Eddington ratio CT AGN hosts were assigned $\text{SFR} = 175 \text{ M}_{\odot} \text{ yr}^{-1}$. The differential counts for this star formation scenario show a large peak $\gtrsim 10 \text{ mJy}$. However, the high Eddington CT AGN account for $> 100\%$ of the local ULIRG range infrared luminosity density measured by Le Floch et al. (2005). If the SFR in high Eddington ratio CT AGN hosts is reduced to $100 \text{ M}_{\odot} \text{ yr}^{-1}$, then AGN will contribute 80% of the local ULIRG range infrared luminosity density, with a larger contribution to the local LIRG range infrared luminosity density. The prominent peak in the differential counts at $\sim 10 \text{ mJy}$ persists, despite the reduced SFR in high Eddington ratio CT AGN. Therefore, a test of the AGN evolution scenario will be if the observed differential counts feature a strong bright end peak, possibly with a knee at moderate fluxes. As a large fraction of the sources contributing to this peak will be CT AGN, the AGN samples used for this test will have to be chosen very carefully.

6. Summary

FIR observations by telescopes like *Herschel* and ALMA will provide important insights on many questions about AGN and their hosts. Determining the flux level at which the differential AGN and host number counts peak will offer crucial constraints to the star formation history of AGN hosts, especially when observing at wavelengths at $\sim 500 \mu\text{m}$. The predictions presented here show that it is likely that the SFR in AGN hosts evolves differently than the SFR in normal galaxies, as indicated by the peak wavelength of the AGN

contribution to the CIRB being significantly longer than the peak wavelength of the CIRB. Understanding how the SFR evolution in active galaxies differs from quiescent galaxies will provide clues on the triggering mechanisms of AGN and how the AGN interacts with the host galaxy. FIR observations will also allow the AGN evolution scenario to be tested by comparing SFRs in bright AGN with different levels of obscuration. The relative contributions of AGN with various levels of obscuration to the bright end differential counts will also be an important test of the major merger trigger model. Applying X-ray stacking techniques to bright 350 or 500 μm sources, especially sources with a hot dust component in the SED, will be an efficient way of finding CT AGN.

The authors thank A. Poglitsch and I. Valtchanov for information on the PACS and SPIRE filters, P. van Hoof for assistance with Cloudy, and the referee for a useful report that helped to improve this paper. This work was supported in part by NSF award AST 1008067.

REFERENCES

- Alexander, D.M., Smail, I., Bauer, F.E., Chapman, S.C., Blain, A.W., Brandt, W.N., & Ivison, R.J., 2005a, *Nature*, 434, 738
- Alexander, D.M., Bauer, F. E., Chapman, S. C., Smail, I., Blain, A. W., Brandt, W. N., & Ivison, R. J., 2005b, *ApJ*, 632, 736
- Alonso-Herrero, A., et al., 2004, *ApJS*, 154, 155
- Altieri, B., et al., 2010, *A&A*, 518, L17
- Amblard, A., et al., 2010, *A&A*, 519 L9
- Antonucci, R., 1993, *ARA&A*, 31, 473
- Ballantyne, D.R. & Papovich, C., 2007, *ApJ*, 660, 988
- Ballantyne, D.R., 2008, *ApJ*, 685, 787
- Ballantyne, D.R., Everett, J.E., & Murray, N., 2006a, *ApJ*, 639, 740
- Ballantyne, D.R., Shi, Y., Rieke, G.H., Donley, J.L., Papovich, C., & Rigby, J.R., 2006b, *ApJ*, 653, 1070
- Berta, S., et al., 2010, *A&A*, 518, L30

- B  thermin, M., Dole, H., Beelen, A., & Aussel, H., 2010, *A&A*, 512, 78
- Bongiovanni,   ., et al., 2010, *A&A*, 519, L4
- Brand, K., et al., 2006, *ApJ*, 644, 143
- Buchanan, C.L., Gallimore, J.F., O’Dea, C.P., Baum, S.A., Axon, D.J., Robinson, A., Elitzur, M., & Elvis, M., 2006, *AJ*, 132, 401
- Daddi, E., et al., 2007, *ApJ*, 670, 173
- Dey, A., et al., 2008, *ApJ*, 677, 943
- Dole, H., et al., 2006, *A&A*, 451, 417
- Donley, J.L., Rieke, G.H., Alexander, D.M., Egami, E., P  rez-Gonz  lez, P.G., 2010, *ApJ*, 719, 1393
- Donley, J.L., Rieke, G.H., P  rez-Gonz  lez, P.G., & Barro, G., 2008, *ApJ*, 687, 111
- Draper, A.R. & Ballantyne, D.R., 2010, *ApJ*, 715, L99
- Draper, A.R. & Ballantyne, D.R., 2009, *ApJ*, 707, 778
- Eales, S., et al., 2010, *PASP*, 122, 499
- Elvis, M., et al., 1994, *ApJS*, 95, 1
- Fadda, D., et al., 2010, *ApJ*, in press
- Ferland, G.J., Korista, K.T., Verner, D.A., Ferguson, J.W., Kingdon, J.B., & Verner, E.M., 1998, *PASP*, 110, 761
- Finkbeiner, D.P., Davis, M., & Schlegel, D.J., 2000, *ApJ*, 544, 81
- Fiore, F., et al., 2009, *ApJ*, 693, 447
- Fiore, F., et al., 2008, *ApJ*, 672, 94
- Franceschini, A., Rodighiero, G., Vaccari, M., Berta, S., Marchetti, L., & Mainetti, G., 2010, *A&A*, 517, 74
- Fu, H., et al., 2010, *ApJ*, in press
- Gandhi, P., Horst, H., Smette, A., H  nig, S., Comastri, A., Gilli, R., Vignali, C., & Duschl, W., 2009, *A&A*, 502, 457

- Georgakakis, A., Rowan-Robinson, M., Nandra, K., Digby-North, J., Pérez-González, P.G., & Barro, G., 2010, MNRAS, 406, 420
- Georgantopolous, I., Rovilos, E., Xilouris, E.M., Comastri, A., & Akylas, A., 2010, A&A, in press
- Ghisellini, G., Haardt, F., & Matt, G., 1994, MNRAS, 267, 743
- Glenn, J., et al., 2010, MNRAS, 409, 109
- Goto, T., et al., 2010a, A&A, 514, 6
- Goto, T., et al., 2010b, MNRAS, in press
- Griffin, M.J., et al., 2010, A&A, 518, L3
- Hasinger, G., 2008, A&A, 490, 905
- Hatziminaoglou, E., et al., 2010, A&A, 518, L33
- Hatziminaoglou, E., Fritz, J., & Jarrett, T.H., 2009, MNRAS, 399, 1206
- Hauser, M.G., et al., 1998, ApJ, 508, 25
- Hinshaw, G., et al., 2009, ApJS, 180, 225
- Holland, W., et al., 2006, SPIE, 6275, 45
- Hönig, S.F., Kishimoto, M., Gandhi, P., Smette, A., Asmus, D., Duschl, W., Polletta, M., & Weigelt, G., 2010, A&A, 515, 23
- Hopkins, P.F., Hernquist, L., Cox, T.J., DiMatteo, T., Robertson, B., & Springel, V., 2006, ApJS, 163, 1
- Hopkins, P.F., Younger, J.D., Hayward, C.C., Narayanan, D., Hernquist, L., 2010, MNRAS, 402, 1693
- Houck, J.R., et al., 2005, ApJ, 622, L105
- Ibar, E., et al., 2010, MNRAS, 409, 38
- Jauzac, M., et al., 2010, A&A, in press
- Juvela, M., Mattila, K., Lemke, D., Klass, U., Leinert, C., & Kiss, C., 2009, A&A, 500, 763

- Kelly, B.C., Vestergaard, M., Fan, X., Hopkins, P., Hernquist, L., & Siemiginowska, A., 2010, *ApJ*, 719, 1315
- Kennicutt, R.C., 1998, *ARA&A*, 36, 189
- Khan, S.A., et al., 2007, *ApJ*, 665, 973
- Kim, M., Ho, L.C., Im, M., 2006, *ApJ*, 642, 702
- Lacey, C. G., Baugh, C. M., Frenk, C. S., Benson, A. J., Orsi, A., Silva, L., Granato, G. L., & Bressan, A., 2010, *MNRAS*, 405, 2
- Laird, E.S., Nandra, K., Pope, A., & Scott, D., 2010, *MNRAS*, 401, 2763
- Lagache, G. & Puget, J.L., 2000, *A&A*, 355, 17
- Laor, A. & Draine, B.T., 1993, *ApJ*, 402, 441
- Le Floch, E., et al., 2005, *ApJ*, 632, 169
- Lutz, D., et al., 2010, *ApJ*, 712, 1287
- Lutz, D., Maiolino, R., Spoon, H.W.W., & Moorwood A.F.M., 2004, *A&A*, 389 93
- Marconi, A., Risaliti, G., Gilli, R., Hunt, L. K., Maiolino, R., & Salvati, M., 2004, *MNRAS*, 351, 169
- Martínez-Sansigre, A., et al., 2009, *ApJ*, 706, 184
- Matsuura, S., et al., 2010, *ApJ*, submitted
- Mazin, D. & Raue, M., 2007, *A&A*, 471, 439
- Mullaney, J. R., Alexander, D. M., Huynh, M., Goulding, A. D., & Frayer, D., 2010, *MNRAS*, 401, 995
- Narayanan, D., et al., 2010, *MNRAS*, 407, 1701
- Netzer, H., et al., 2007, *ApJ*, 666, 806
- Oliver, S.J., et al., 2010, *A&A*, 518, L21
- Page, M.J., Stevens, J.A., Ivison, R.J., Carrera, F.J., 2004, 611, L85
- Papovich, C., et al., 2004, *ApJS*, 154, 70

- Parra, R., Conway, J.E., Aalto, S., Appleton, P.N., Norris, R.P., Pihlström, Y.M., & Kewley, L.J., 2010, *ApJ*, 720, 555
- Pascale, E., et al., 2010, *MNRAS*, submitted
- Patanchon, G., et al., 2009, *ApJ*, 707, 1750
- Persson, C.M., et al., 2007, *A&A*, 476, 807
- Pilbratt, G.L., et al., 2010, *A&A*, 518, L1
- Poglitsch, A., et al., 2010, *A&A*, 518, L2
- Rieke, G.H., Alonso-Herrero, A., Weiner, B.J., Pérez-González, P.G., Blaylock, M., Donley, J.L., & Marcillac, D., 2009, *ApJ*, 692, 556
- Rigby, J.R., et al., 2004, *ApJS*, 154, 160
- Rigopoulou, D., et al., 2009, *MNRAS*400, 1199
- Roseboom, I.G., et al., 2010, *MNRAS*, 409, 48
- Rubio, M., Paron, S., & Dubner, G., 2009, *A&A*, 505, 177
- Sanders, D.B., Soifer, B.T., Elias, J.H., Madore, B.F., Matthews, K., Neugebauer, G., & Scoville, N.Z., 1988, *ApJ*, 325, 74
- Serjeant, S., et al., 2010, *A&A*, 518 L7
- Silva, L., Maiolino, R., & Granato, G.L., 2004, *MNRAS*, 355, 973
- Soifer, B.T., Helou, G., & Werner M., 2008, *ARA&A*, 46, 201
- Steffen, A.T., Strateva, I., Brandt, W.N., Alexander, D.M., Koekemoer, A.M., Lehmer, B.D., Schneider, D.P., & Vignali, C., 2006, *AJ*, 131, 2826
- Sturm, E., et al., 2010, *A&A*, 518, L36
- Treister, E., Urry, C.M., & Virani, S., 2009a, *ApJ*, 696, 110
- Treister, E., et al., 2009b, *ApJ*, 706, 535
- Treister, E., Urry, C.M., Schawinski, K., Cardamone, C.N., & Sanders, D.B., 2010, *ApJ*, in press
- Ueda, Y., Akiyama, M., Ohta, K., & Miyaji, T., 2003, *ApJ*, 598, 886

- Veilleux, S., Kim, D.-C., Sanders, D. B., Mazzarella, J. M., & Soifer, B. T., 1995, *ApJS*, 98, 171
- Weedman, D.W., Le Floch, E., Higdon, S.J.U., Higdon, J.L., & Houck, J.R., 2006, *ApJ*, 638, 613
- Weingartner, J.C. & Murray, N., 2002, *ApJ*, 580, 88
- Werner, M.W., et al., 2004, *ApJS*, 154, 1
- Wilman, R.J., Jarvis, M.J., Mauch, T., Rawlings, S., & Hickey, S., 2010, *MNRAS*, 405, 447
- Yan, L., et al., 2005, *ApJ*, 628, 604
- Yuan, T.-T., Kewley, L.J., & Sanders, D.B., 2010, *ApJ*, 709, 884

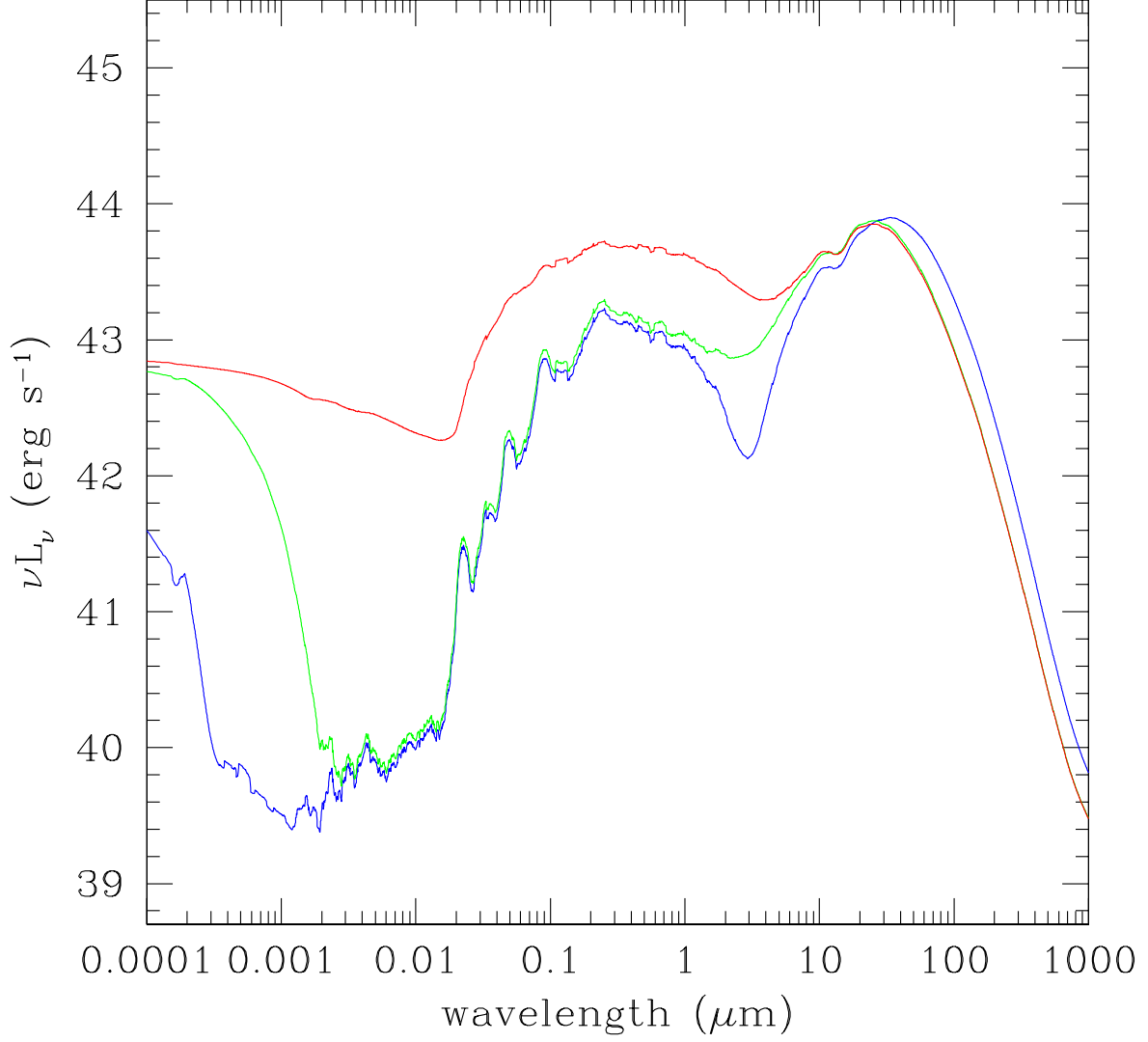


Fig. 1.— Rest frame SEDs for high Eddington ratio AGN ($L/L_{Edd} > 0.9$) with $\log L_X = 43$ and $z = 0.45$ ($f_{CT} = 0.86$ and $f_2 = 0.78$). The type 1 SED is shown in red, the type 2 SED is shown in green, while the Compton thick SED is shown in blue.

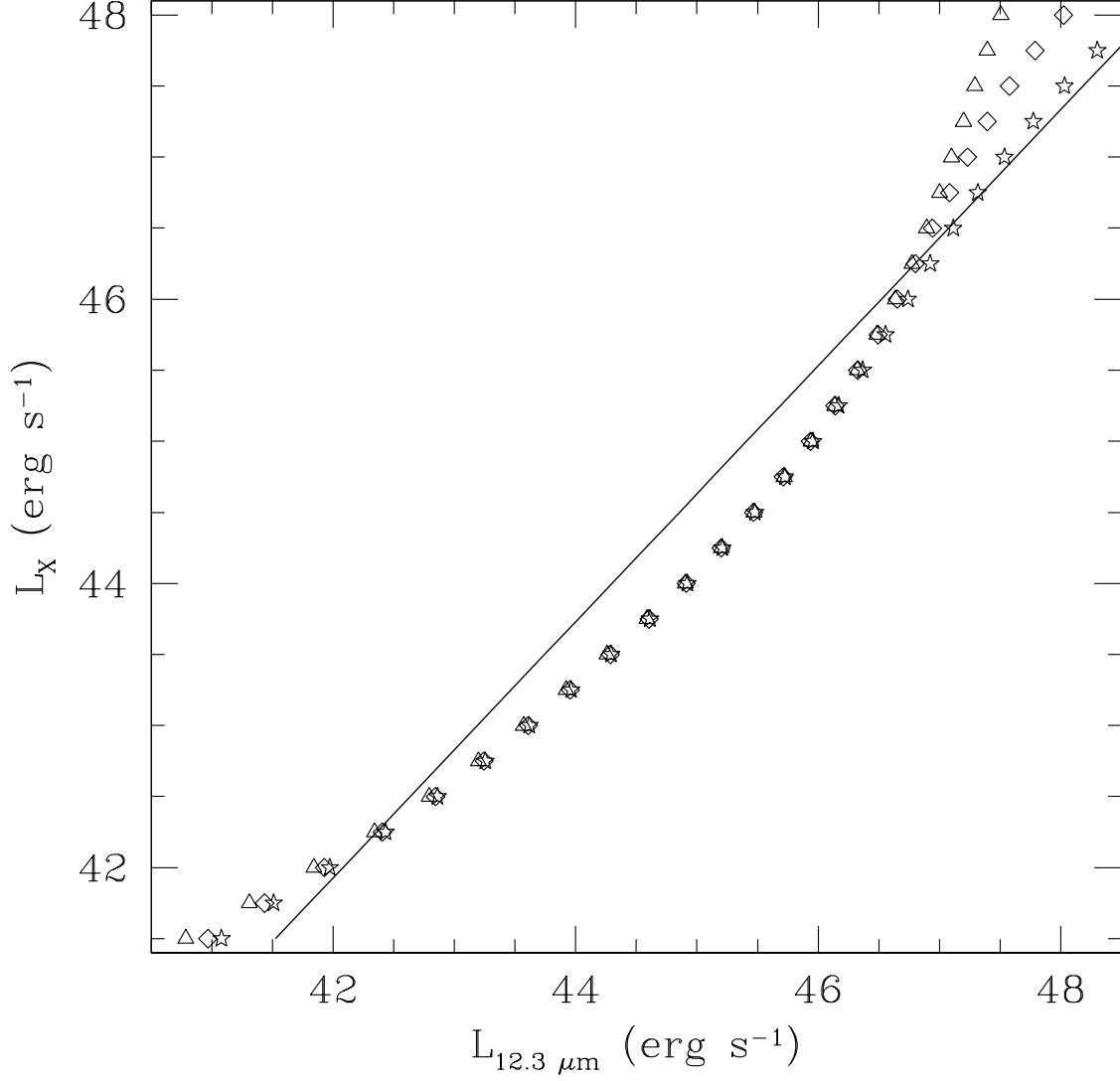


Fig. 2.— L_X versus $L_{12.3 \mu m}$ for the high Eddington ratio ($L/L_{Edd} > 0.9$) model SEDs at $z = 0.05$. Type 1 SEDs are shown as stars, type 2 SEDs are shown as diamonds, and the Compton thick SEDs are shown as triangles. The black line is the best-fit line for the well-resolved sample of Gandhi et al. (2009).

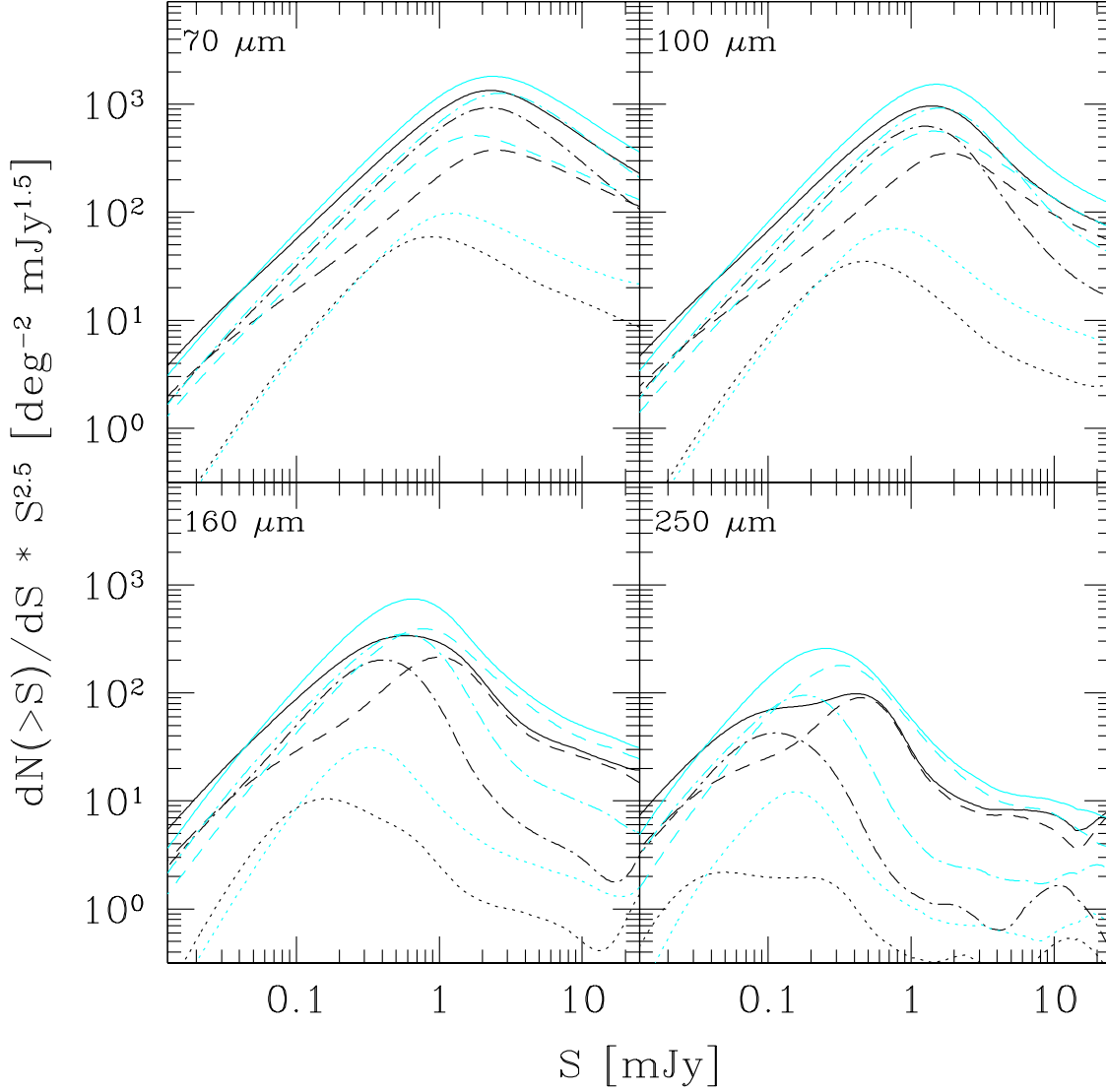


Fig. 3.— Euclidean normalized differential number counts for bare AGN at 70, 100, 160, and 250 μm . The black lines plot the predictions based on the composite model of Draper & Ballantyne (2010) and the cyan lines show the predictions for the original model. The dotted-lines are predictions for type 1 AGN, the dot-dashed lines are predictions for type 2 AGNs, and the dashed lines are predictions for Compton thick AGN.

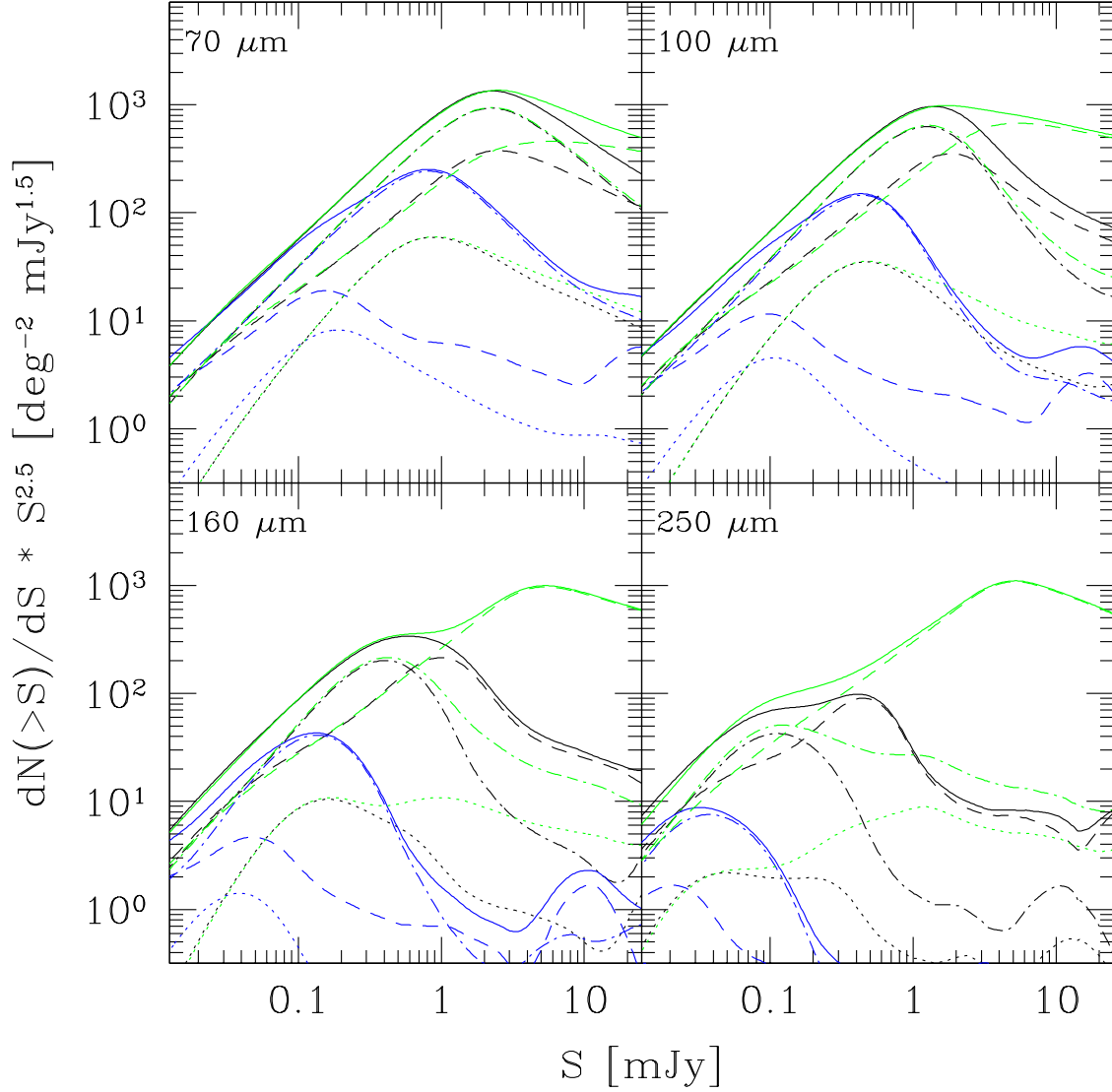


Fig. 4.— Comparison of Euclidean normalized differential number counts for bare AGN at 70, 100, 160, and 250 μm using the composite model. The blue lines are $r = 1$ pc and $n_{H,CT} = 10^6 \text{ cm}^{-3}$, the black lines are $r = 10$ pc and $n_{H,CT} = 10^6 \text{ cm}^{-3}$, and the green lines are $r = 10$ pc and $n_{H,CT} = 10^4 \text{ cm}^{-3}$. The line styles are the same as in figure 3.

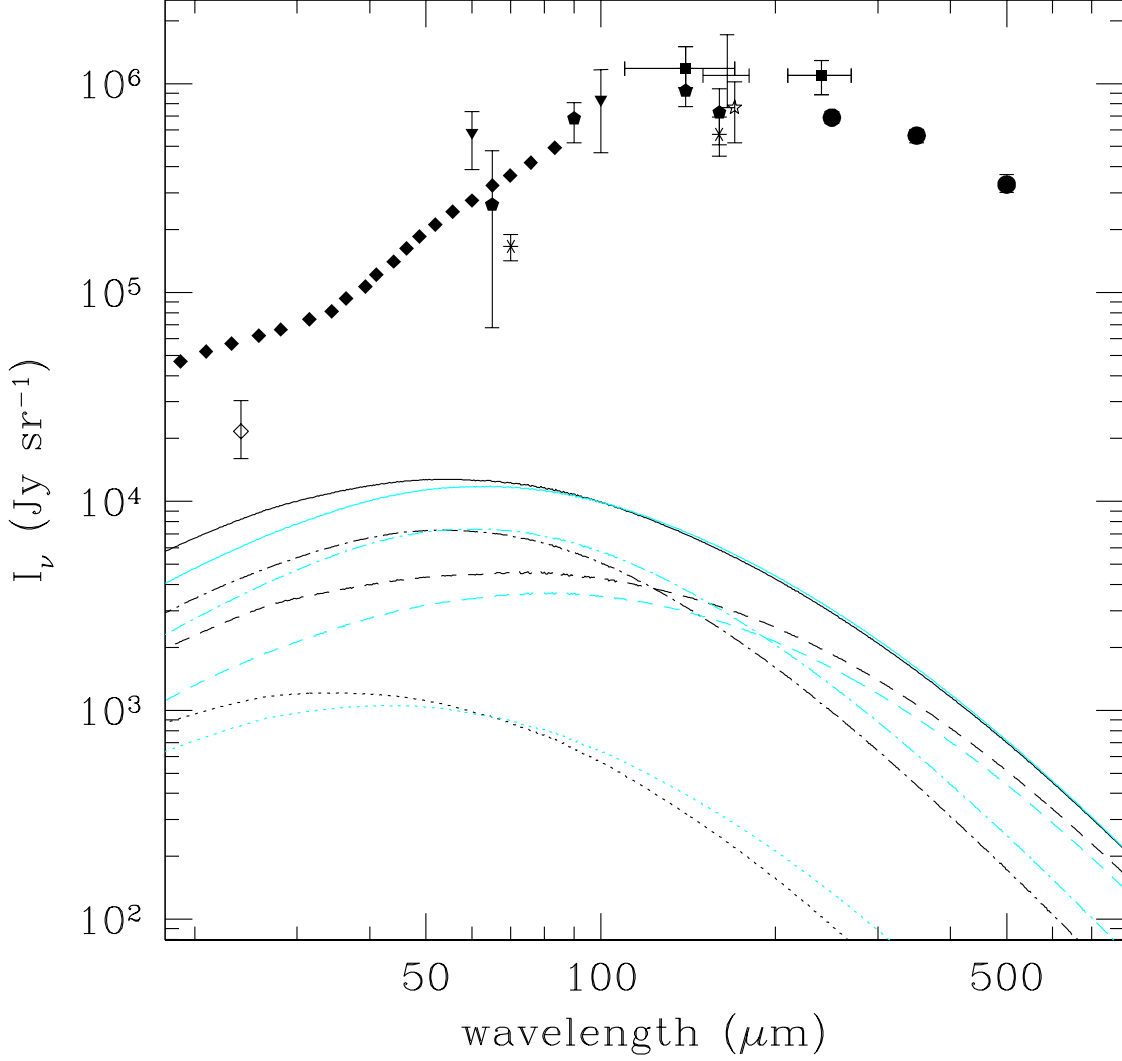


Fig. 5.— Bare AGN contribution to the CIRB. Line color and styles are the same as in figure 3. Data points are from a variety of instruments: the filled diamonds are from IACTS (Mazin & Raue 2007); the open diamond is from MIPS (Papovich et al. 2004); the triangles are from DIRBE (Finkbeiner et al. 2000); the pentagons are from AKARI (Matsuura et al. 2010); the asterisks are from MIPS (Dole et al. 2006); the squares are from DIRBE (Hauser et al. 1998); the cross is from ISOPHOT (Juvela et al. 2009); the star is also from ISOPHOT (Lagache & Puget 2000); and the circles are from BLAST (Patanchon et al. 2009).

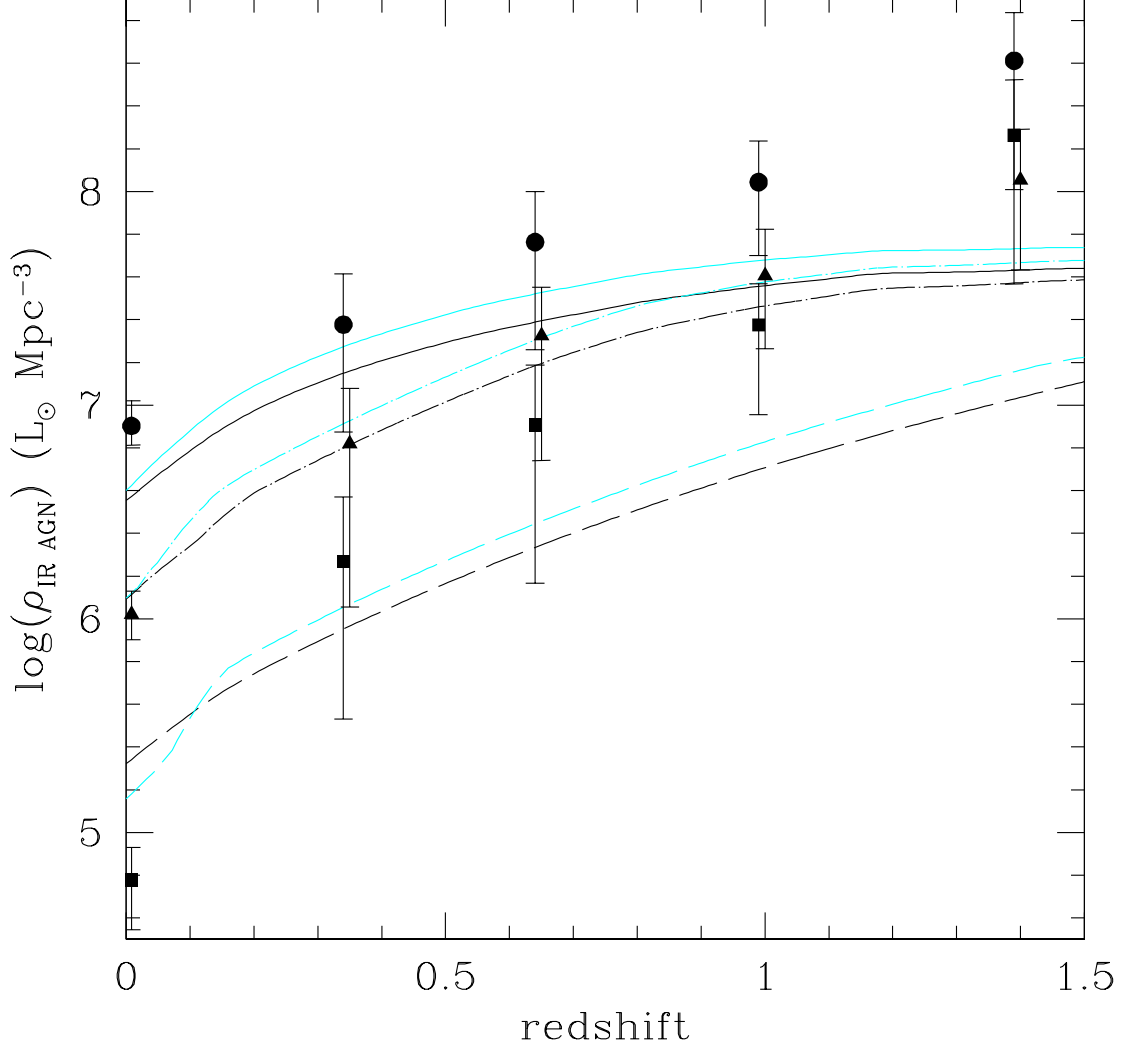


Fig. 6.— Infrared luminosity density of bare AGN with respect to redshift. Solid lines and circles refer to ρ_{IR} , dot-dashed lines and triangles refer to $\rho_{\text{IR}}^{\text{LIRG}}$, while dashed lines and squares refer to $\rho_{\text{IR}}^{\text{ULIRG}}$. The black lines show the composite model and the cyan lines show the original model. The $z = 0.0082$ data points are taken from Goto et al. (2010b) and the higher redshift data points are from the work of Goto et al. (2010a) in the AKARI NEP deep field.

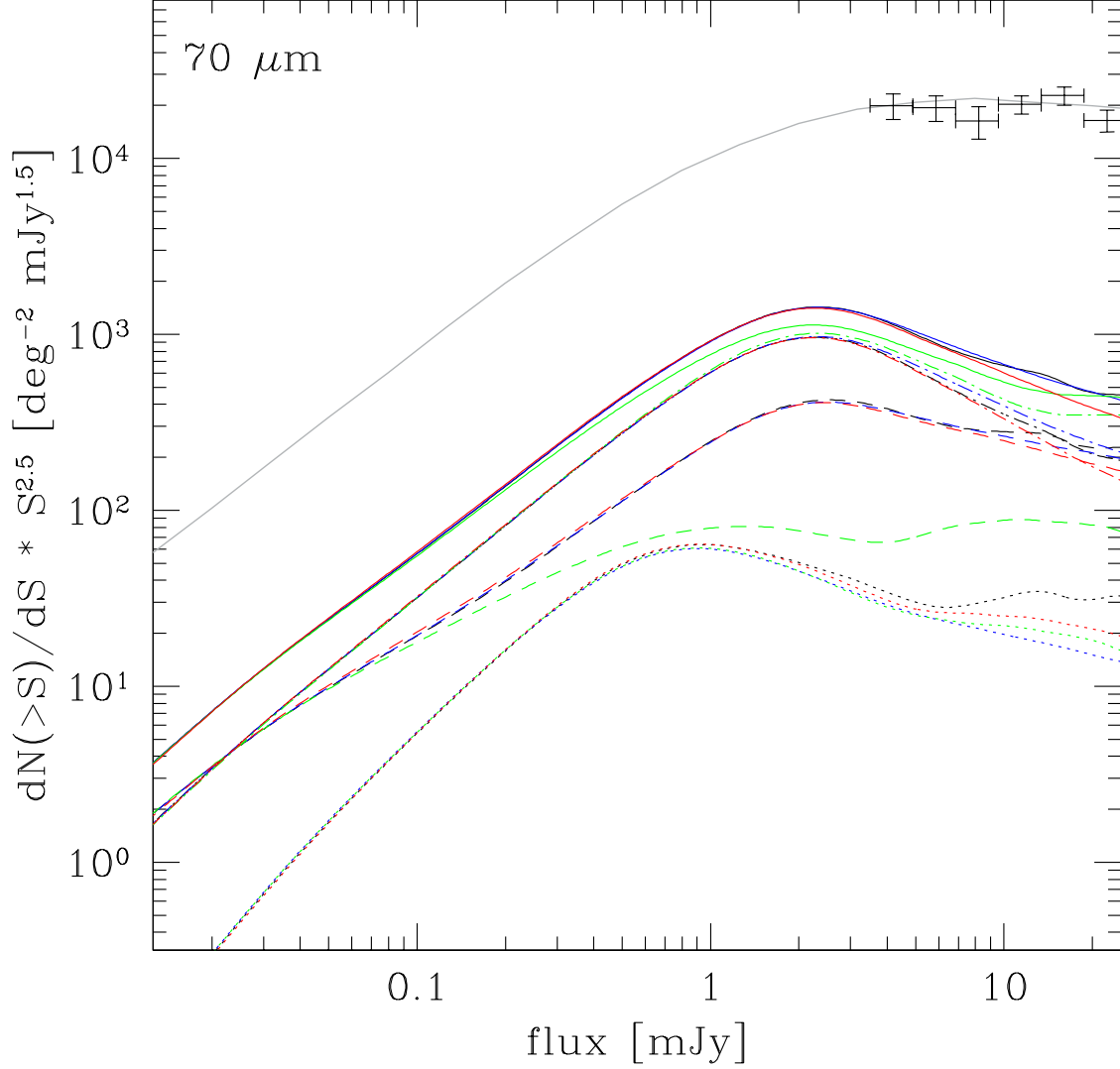


Fig. 7.— Euclidean normalized differential number counts for AGN and host star formation at $70 \mu\text{m}$ for the various star formation scenarios using the composite model. Constant star formation is shown as black. The AGN evolution star formation scenario is shown as green. Star formation with the redshift evolution found by Serjeant et al. (2010) is shown as red. The star formation scenario using the redshift and AGN L_X evolution by Wilman et al. (2010) is shown in blue. The line styles are the same as in figure 3. The grey line shows the best fit model galaxy differential number counts of Franceschini et al. (2010). *Spitzer* data points are from Béthermin et al. (2010).

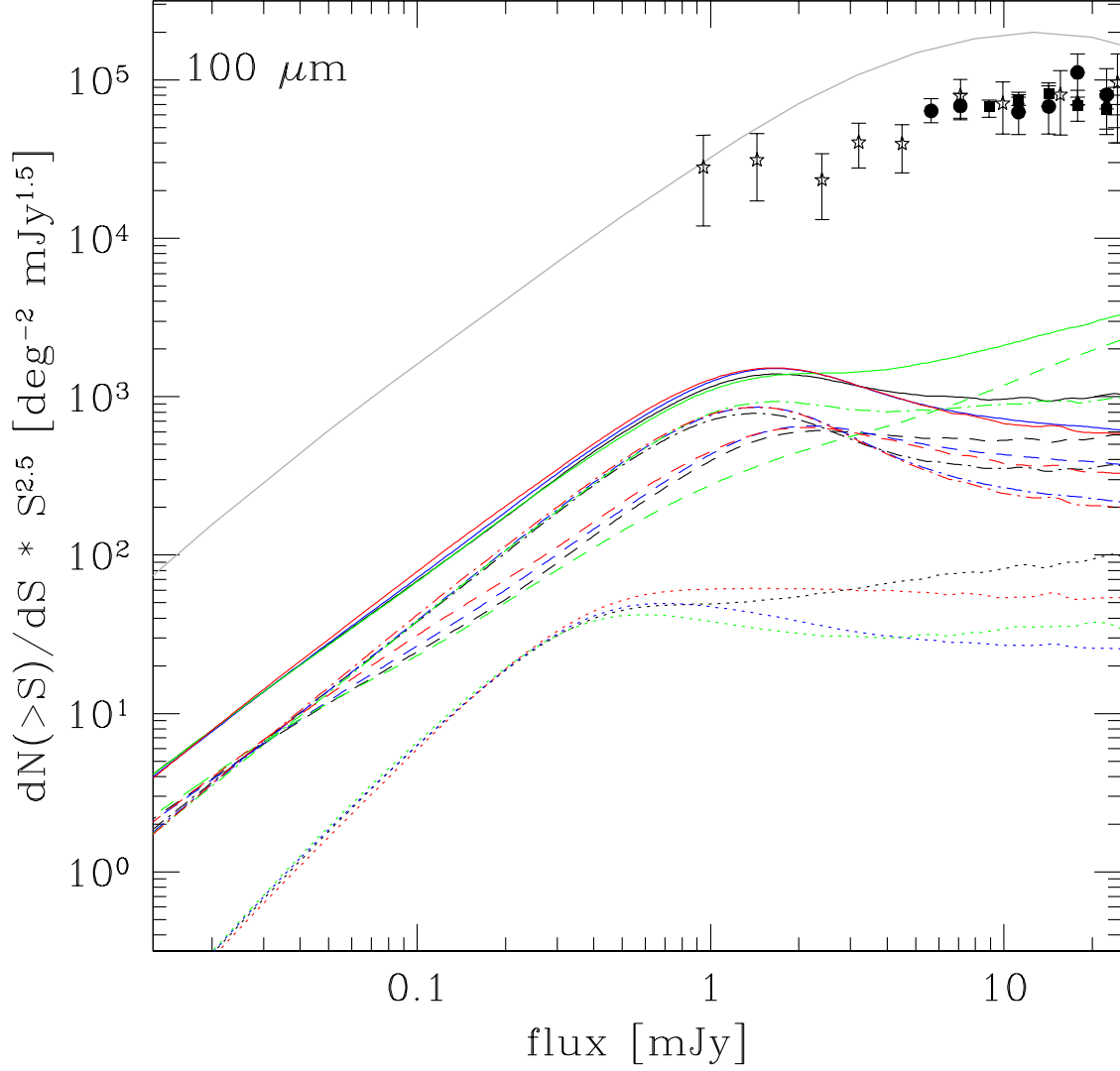


Fig. 8.— Euclidean normalized differential number counts for AGN and host star formation at 100 μm for the various star formation scenarios using the composite model. Lines are the same as in figure 7. *Herschel* data points are from Altieri et al. (2010) (stars) and Berta et al. (2010) (circles—GOODS-N, squares—Lockman XMM, and triangles—COSMOS).

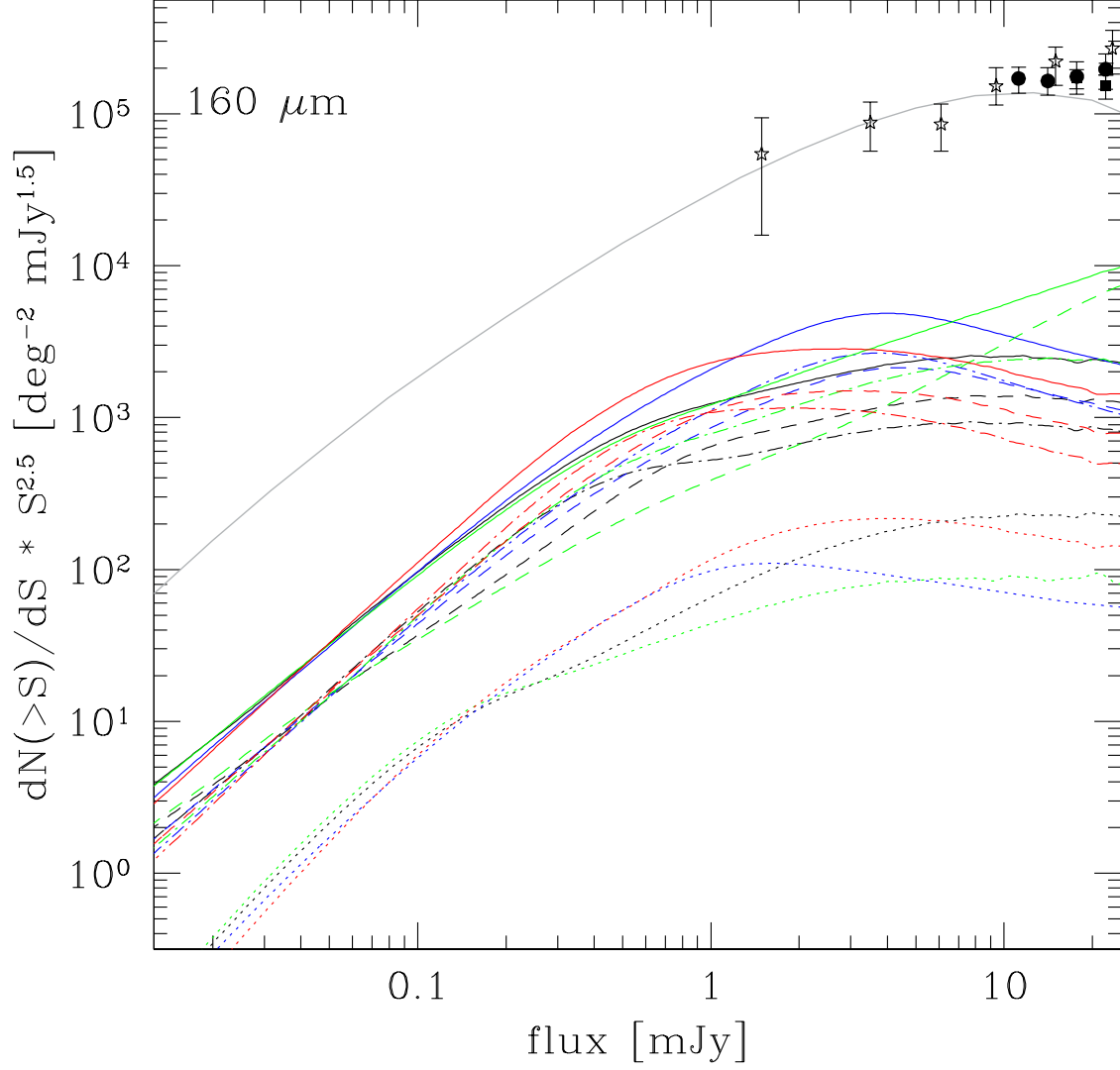


Fig. 9.— Euclidean normalized differential number counts for AGN and host star formation at $160 \mu\text{m}$ for the various star formation scenarios using the composite model. Line colors and styles are the same as in figure 7. Data points are the same as in figure 8.

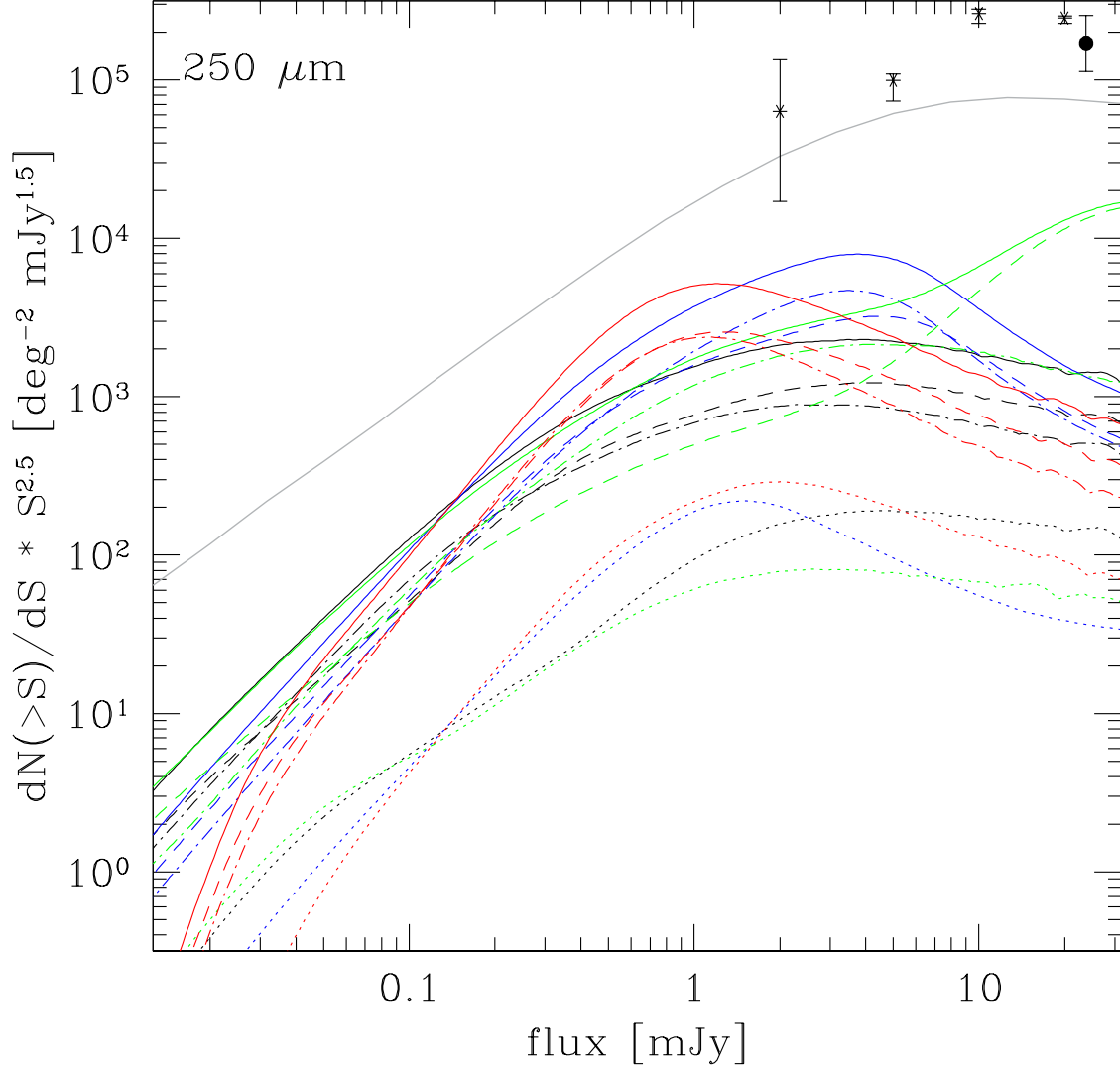


Fig. 10.— Euclidean normalized differential number counts for AGN and host star formation at 250 μm for the various star formation scenarios using the composite model. Line colors and styles are the same as in figure 7. Circles are data points from *Herschel* (Oliver et al. 2010) and astrisks show the multiply-broken power-law model of Glenn et al. (2010).

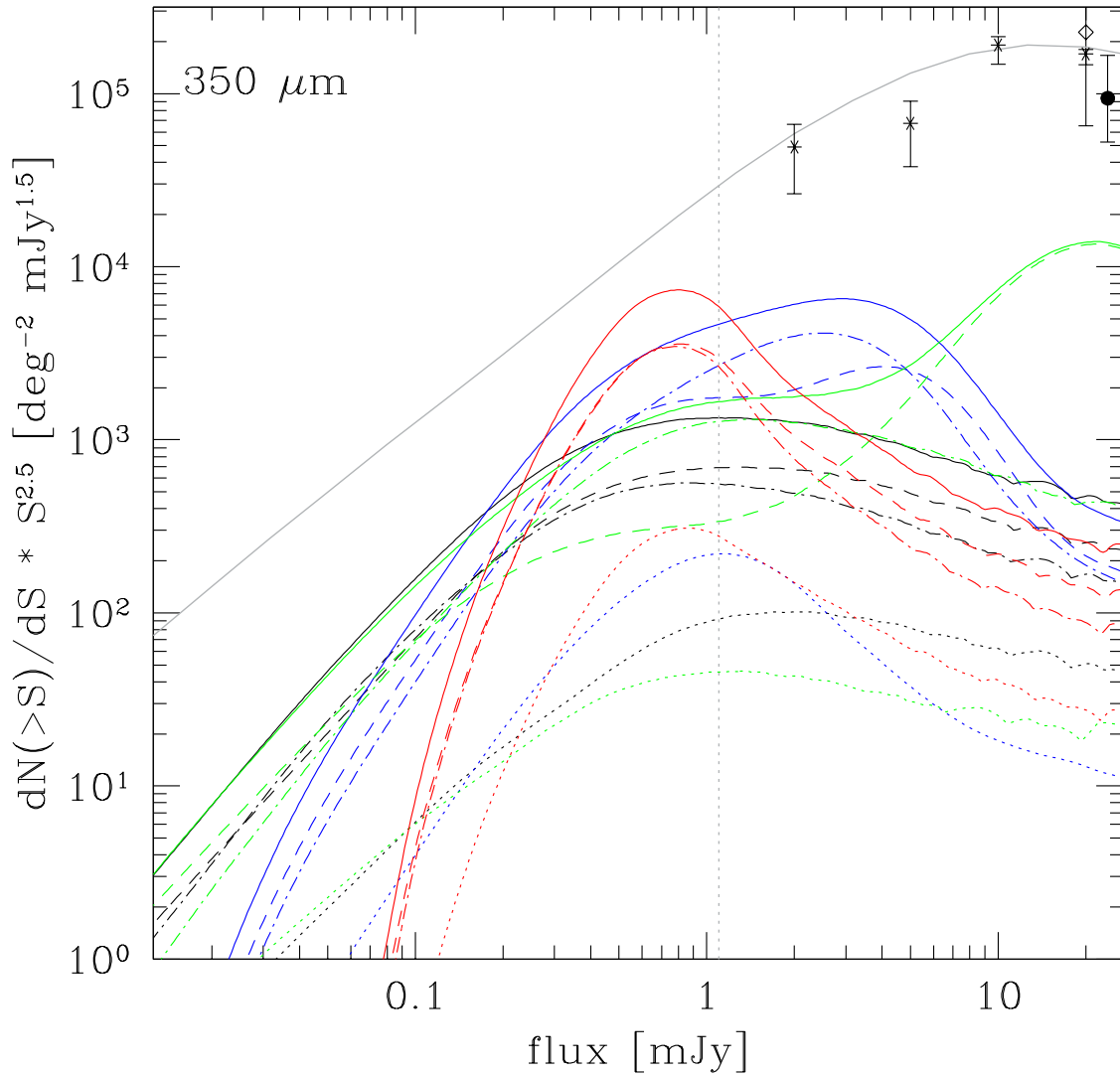


Fig. 11.— Euclidean normalized differential number counts for AGN and host star formation at 350 μm for the various star formation scenarios using the composite model. Line colors and styles are the same as in figure 7. Additionally, the dotted grey line shows the expected continuum sensitivity of ALMA for an integration time of 60 seconds and a spectral resolution of 1 km/s. Circles are data points from *Herschel* (Oliver et al. 2010), the diamond is from SHARC II (Khan et al. 2007), and astrisks show the multiply-broken power-law model of Glenn et al. (2010).

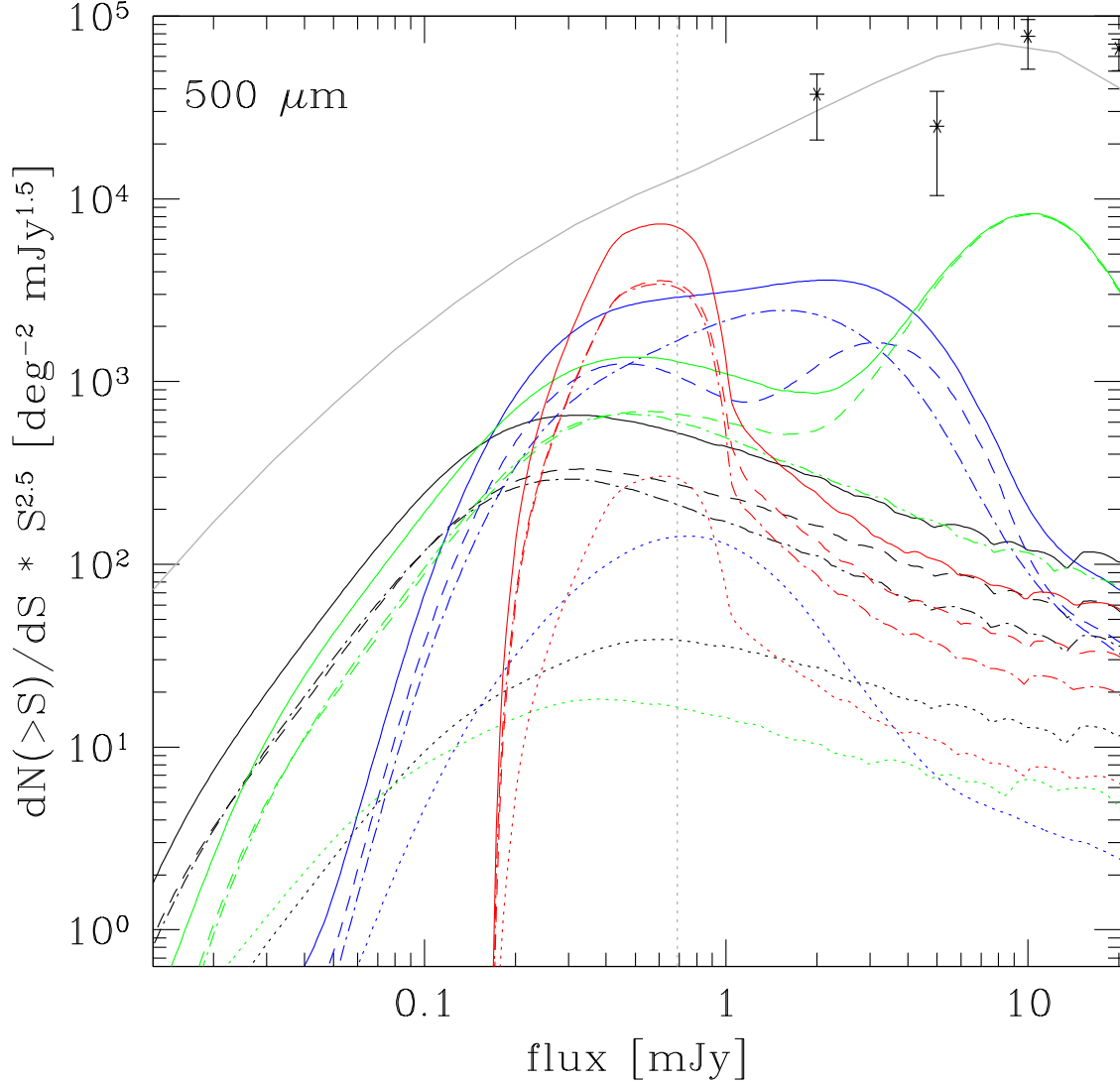


Fig. 12.— Euclidean normalized differential number counts for AGN and host star formation at 500 μm for the various star formation scenarios using the composite model. Line colors and styles are the same as in figure 11. Circles are data points from *Herschel* (Oliver et al. 2010) and astrisks show the multiply-broken power-law model of Glenn et al. (2010). At bright fluxes numerical artifacts are present due to the small number of sources in this flux region.

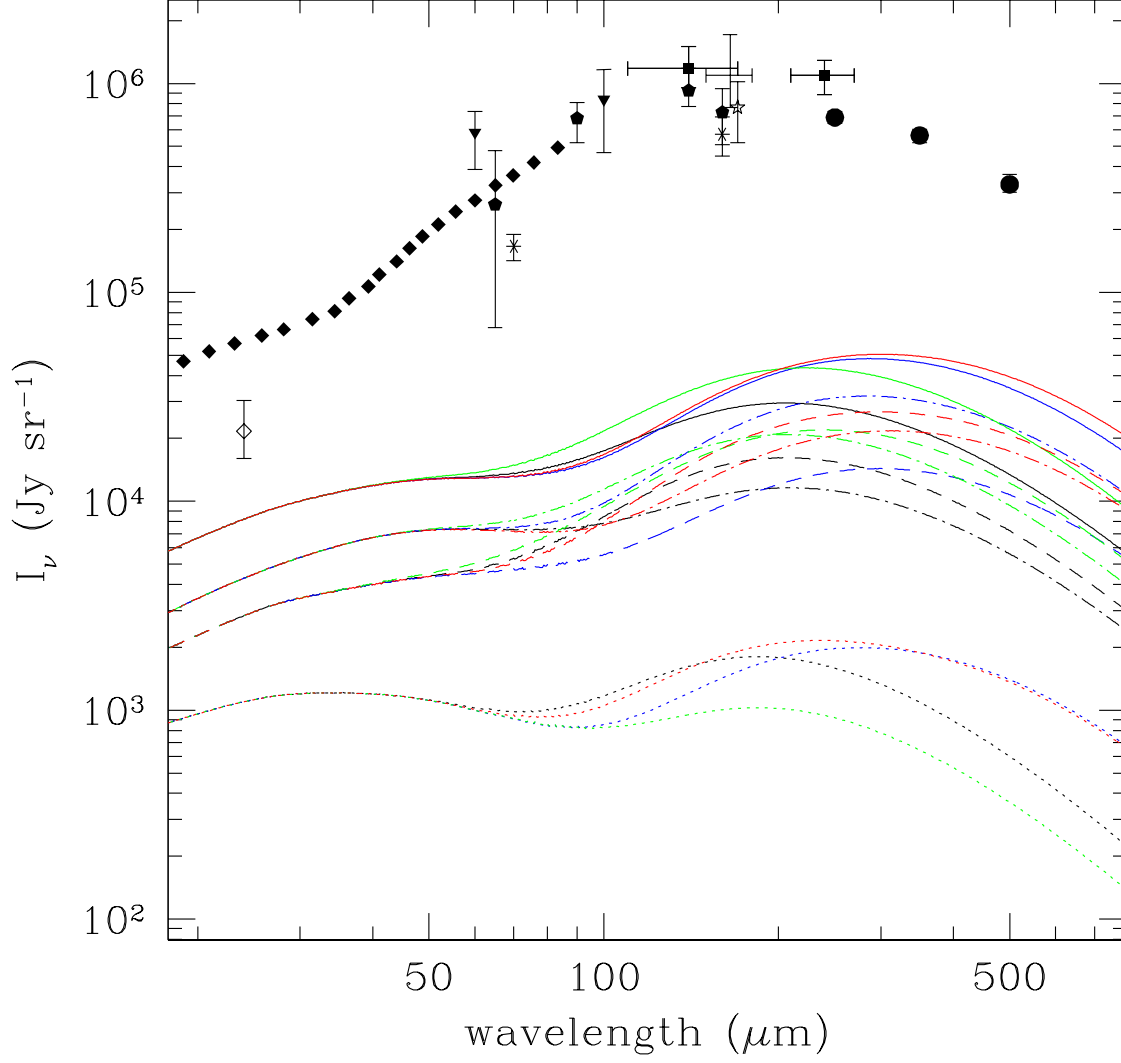


Fig. 13.— AGN and host star formation contribution to the CIRB for the various star formation scenarios using the composite model. Line colors are the same as in figure 8. The line styles are the same as in figure 3. Data points are the same as figure 5.

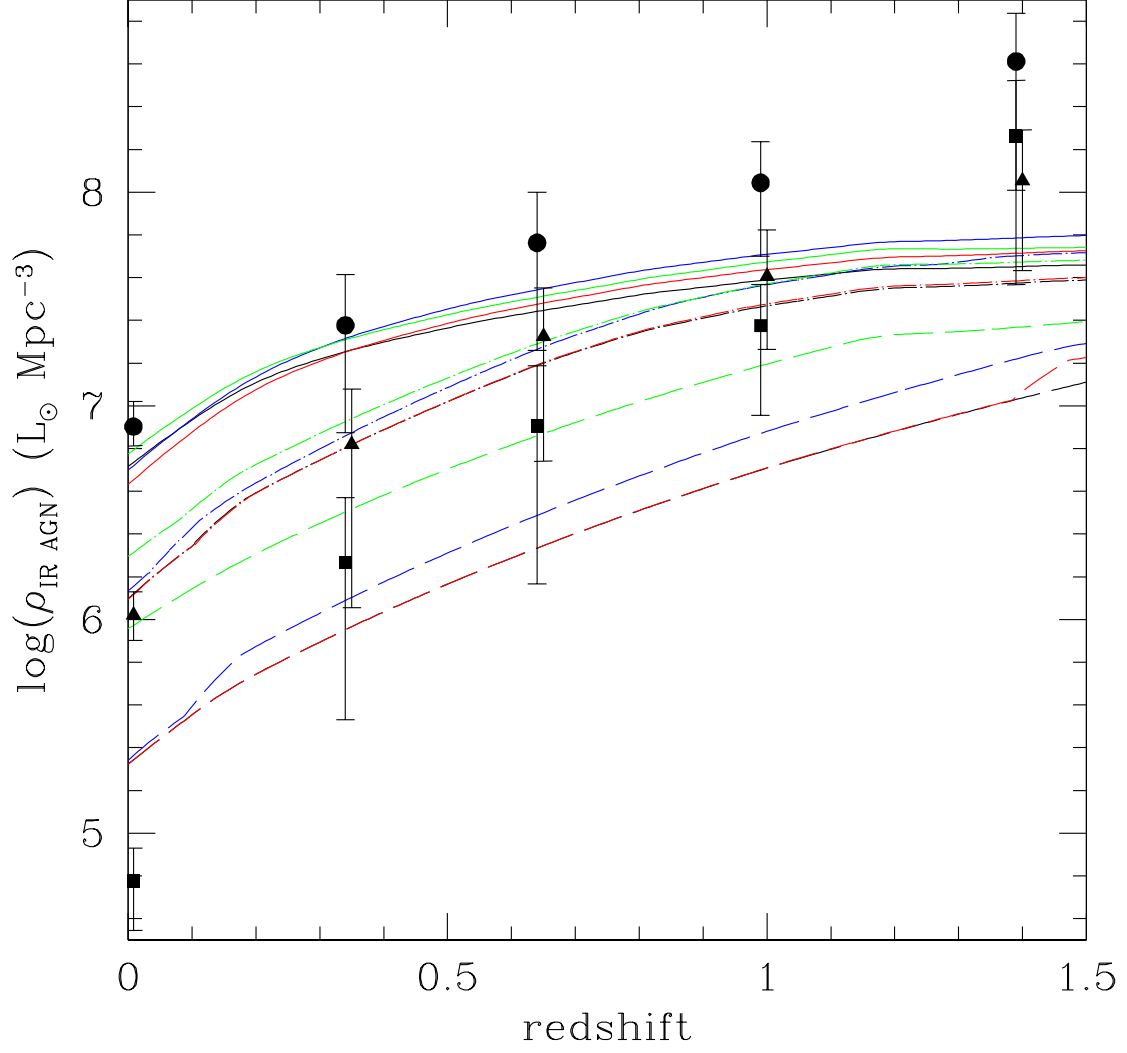


Fig. 14.— AGN and host star formation infrared luminosity density for the various star formation scenarios using the composite model. Line colors are the same as in figure 8. The line styles and data points are the same as figure 6.

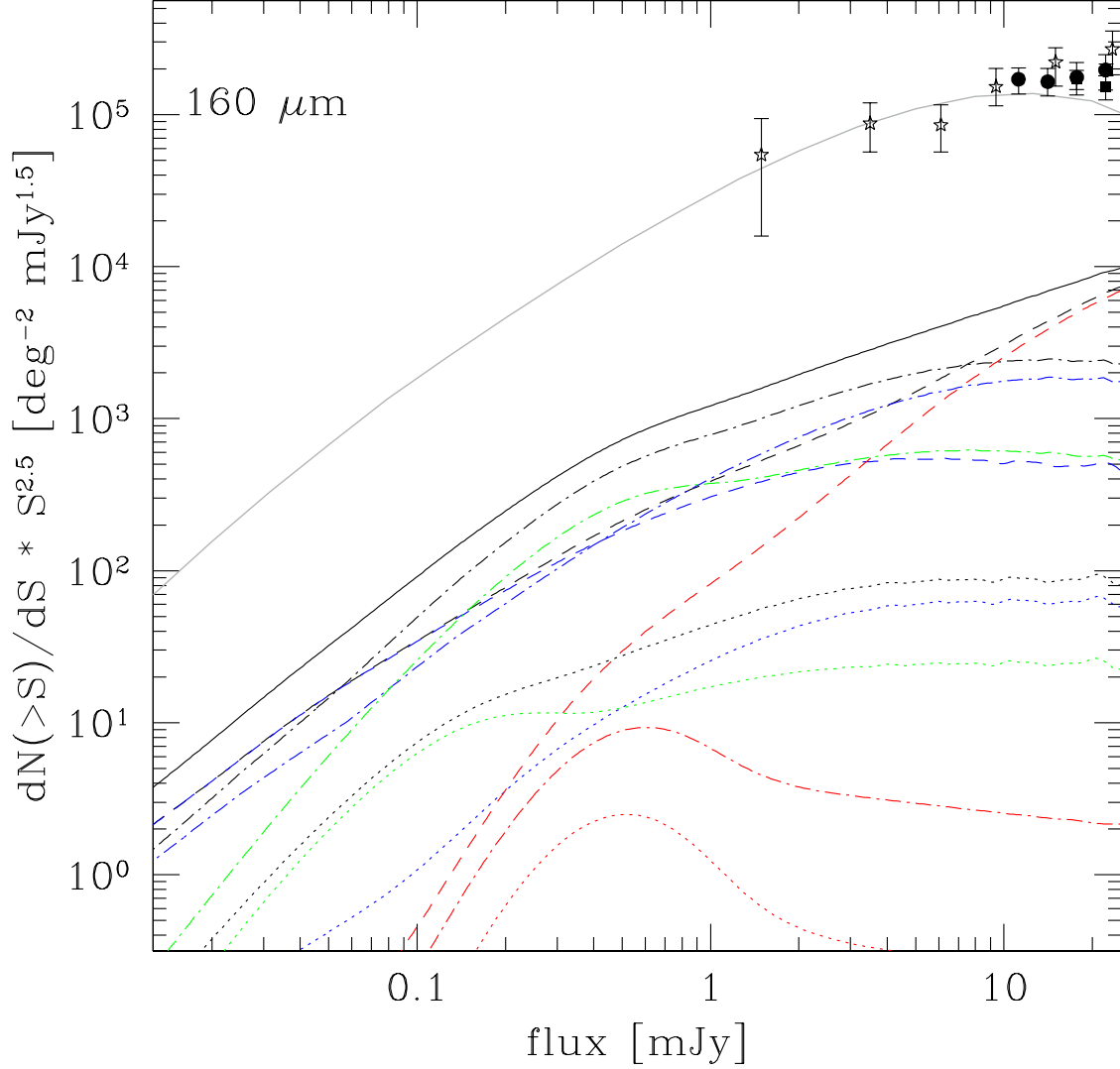


Fig. 15.— Euclidean normalized differential number counts for AGN and host star formation at $160\ \mu\text{m}$ for the AGN evolution star formation model. Black lines show the total predictions for the composite model with the low Eddington ratio sources in blue, the mid Eddington ratio sources in green, and the high Eddington ratio sources in red. The line styles are the same as in figure 3. The solid grey lines shows the best fit model galaxy differential number counts of Franceschini et al. (2010). the Data points are the same as in figure 7.

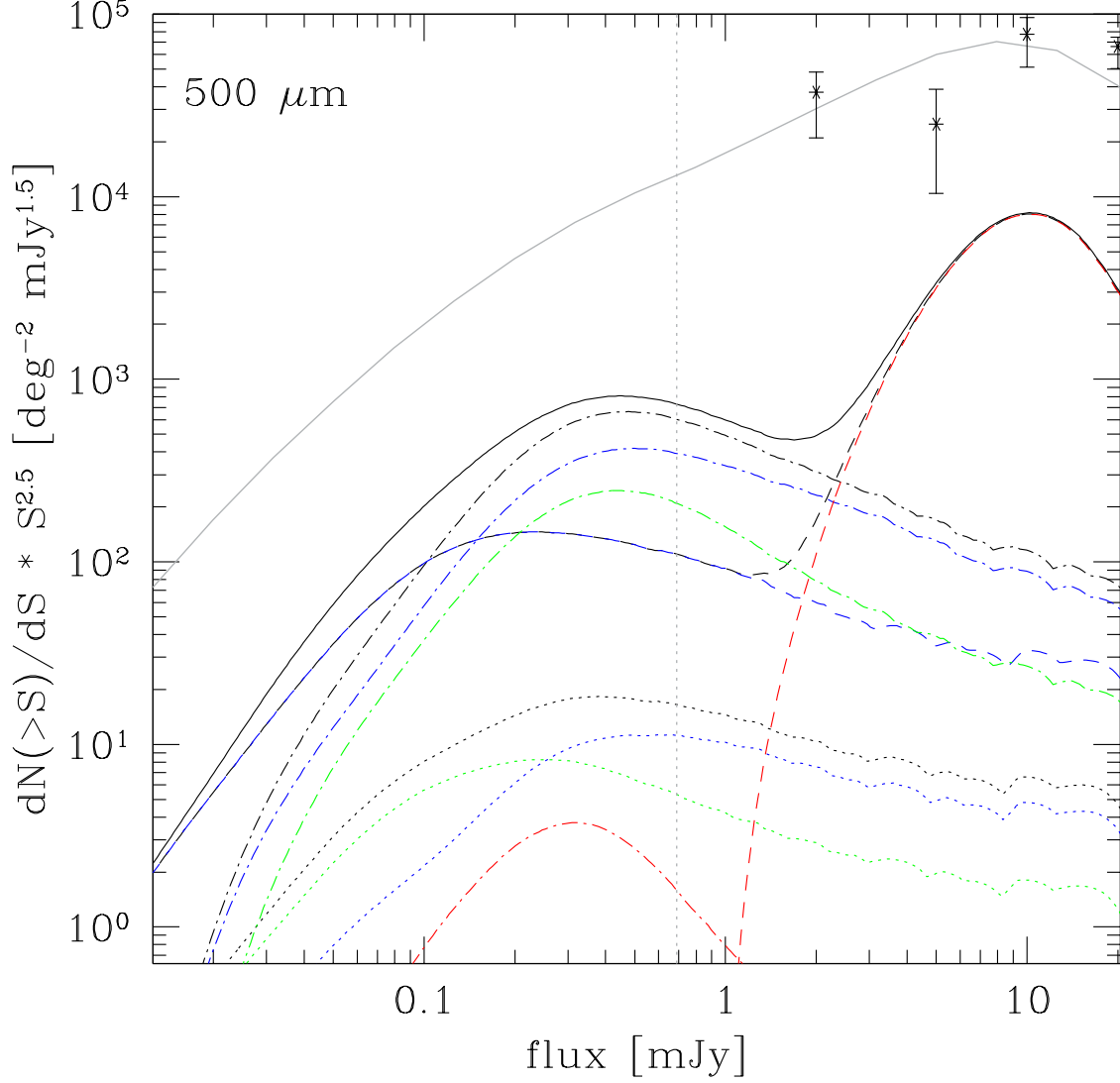


Fig. 16.— Euclidean normalized differential number counts for AGN and host star formation at $160 \mu\text{m}$ for the AGN evolution star formation model. Line colors and styles are the same as in figure 15 with the addition of the dotted grey line which shows the expected continuum sensitivity of ALMA for an integration time of 60 seconds and a spectral resolution of 1 km/s. Data points are the same as in figure 10. At bright fluxes numerical artifacts are present due to the small number of sources in this flux region.